INTERTIDAL MIXING ZONE DYNAMICS AND SWASH INDUCED INFILTRATION IN A SANDY BEACH AQUIFER, CAPE HENLOPEN, DELAWARE

by

James W. Heiss

A thesis submitted to the Faculty of the University of Delaware in partial fulfillment of the requirements for the degree of Master of Science in Geology

Summer 2011

INTERTIDAL MIXING ZONE DYNAMICS AND SWASH INDUCED INFILTRATION IN A SANDY BEACH AQUIFER, CAPE HENLOPEN, DELAWARE

by

James W. Heiss

Approved: _____
Holly A. Michael, Ph.D.
Professor in charge of thesis on behalf of the Advisory Committee

Approved: _____
Susan McGeary, Ph.D.
Chair of the Department of Geological Sciences

Approved: _____
Nancy M. Targett, Ph.D.
Dean of the College of Earth, Ocean, and Environment

Approved: _____
Charles G. Riordan, Ph.D.
Vice Provost for Graduate and Professional Education

ACKNOWLEDGMENTS

I would like to first thank my advisor, Dr. Holly Michael, for her guidance, insight, and encouragement throughout the course of this research. I would also like to thank my thesis committee, Dr. William Ullman and Dr. Thomas McKenna for their thoughtful input, suggestions, and assistance when it was most needed. To my lab members, I have benefited greatly from your moral and intellectual support.

Field Assistance

A number of people have assisted with instrumentation and field work and for that I extend my sincerest gratitude.

Lindsay Byron: 2009-2010

Helen Simmons: July-August 2009

Shaun Smith: November 2009

Jillian Harig: April 2010, October 2010, March 2011

Andrew Musetto: July 2010, March 2011

Ellen McGuiness: July 2010

David Wessell: April 2011

DEDICATION

This thesis is dedicated to my parents for providing me with a loving environment and who have bestowed me with a great deal of support, encouragement, and inspiration.

TABLE OF CONTENTS

LIST OF TABLES

LIST OF FIGURES

ABSTRACT

Submarine groundwater discharge has been shown to be an important source of nutrients, heavy metals, and organic compounds to the coastal ocean. Physical flow and mixing dynamics in the intertidal zone may influence these contaminant fluxes; however the mechanisms that contribute to the spatial and temporal dynamics of mixing of saltwater and through-flowing freshwater are not well understood. Flow systems in two shallow beach aquifers at Cape Henlopen, DE were characterized over multiple time scales using multilevel porewater samplers, pressure transducers, and moisture sensors. Porewater samples indicate the presence of a saline groundwater circulation cell beneath the beachface that is formed by seawater infiltrating across the upper beachface, which then circulates downward and seaward before discharging farther offshore. The circulation cell deepens and its areal extent increases when forced with a larger tidal amplitude. Longer term monitoring shows that higher inland water tables during spring and the resultant increase in freshwater forcing cause the circulation cell to freshen while lower inland water tables associated with winter result in a well-developed density inversion.

A study of swash-induced infiltration was performed to quantify the effects of swash zone width and tidal elevation on the flux of seawater into the beach aquifer. High-frequency pressure and soil moisture measurements from shore-perpendicular

arrays across the beachface were used to infer influx rates. Direct measurement of moisture content in the unsaturated zone and capillary fringe is needed to infer fluxes due to moisture conditions above the water table that are not measured by the pressure sensors. Infiltration occurred during the rising tide at the leading edge of the swash zone and increased in magnitude from low tide to high tide. Infiltration rates were on average 2.2 times greater near mean higher high water than near mean lower low water. Measurements revealed that swash zone width influences infiltration: influx rates associated with a beach with a wider swash zone were 2.7 times higher than those of a beach with a narrower swash zone. These insights into beach groundwater dynamics have implications for estimating fluid and chemical fluxes to coastal waters.

Chapter 1

INTRODUCTION

An increasing portion of the world's coastal ecosystems are being threatened by eutrophication caused by nutrient contaminants from agricultural and urban runoff. Although stream and river discharge has been shown to deliver a significant portion of nutrient loads to near-shore systems, submarine groundwater discharge (SGD) has received increased attention as it has been recognized that it also serves as an important pathway for chemical transport (Taniguchi, 2002).

SGD that is rich in nutrients due to contamination of water table aquifers can result in eutrophication. Although SGD is a natural process, the levels of nutrients and therefore nutrient loads associated with SGD may be increased by domestic, municipal, agricultural, and industrial waste disposal processes leading to elevated levels of primary production, anoxic conditions, habitat degradation, and alteration in the structure and function of food webs (Paerl et al., 2003). SGD is also an important source of other materials including radionuclides, metals, and organic compounds to the ocean; however chemical transformations in the beach subsurface can moderate net fluxes of these dissolved contaminants from the beach aquifer. Yet few studies have reported on the hydrologic mechanisms that control the geometry of the beach aquifer and the interaction between beach water masses with contrasting geochemical

characteristics. Freshwater and seawater mixing and the hydrologic factors that enhance beach groundwater circulation are crucial for understanding beach reactivity, chemical ocean budgets, and the extent to which beaches are threatened in the face of sea-level rise.

The effects of tidal and wave forcing on beach aquifer response has been well documented in the field (e.g. Turner and Nielsen, 1997; Austin and Masselink, 2006; Li et al., 2006; Li and Boufadel, 2010) and a number studies (e.g. Robinson et al. 2006 and Robinson et al. 2007b) have used field measurements in conjunction with numerical models to provide insight into the time scales associated with mixing of fresh and saltwater.

The action of tides on the beachface leads to the formation of a mixing zone with circulating seawater caused by waves and tides. Recent studies (Nielsen, 1990; Ataie-Ashtiani, 2001; and Robinson et al., 2006), have suggested that tidal forcing and subsequent mixing and oscillation of the water table provides an important driving mechanism to subsurface flow, alters beach morphology, and significantly affects rates of SGD from the beach aquifer. Henderson et al. 2010 used time-lapse electrical resistivity imaging of the beach aquifer to conclude that oceanic oscillations can control the discharge of freshwater to the coastal zone.

In addition to tidal forcing, wave swash contributes to the formation of the circulation cell. Previous studies (e.g. Turner and Nielsen, 1997; Turner and Masselink, 1998; Baldock et al., 2001; Cartwright et al., 2006) have linked swash induced beach groundwater flow and wave energy dissipation to bed fluidization and

sediment transport. Other investigations (e.g. Turner and Nielsen, 2007; Horn et al., 2003; Blewett et al., 2001; Baldock et al., 2001; Turner, 1998) have verified the presence of high-frequency swash induced water table fluctuations.

Santos et al. (2000) and Santoro (2010) provide a framework for evaluating the importance of beaches on regulating chemical ocean budgets by analyzing nutrient concentrations in porewater samples and found that temporally variable biogeochemical conditions beneath the beachface can lead to nutrient discharges that fluctuate over time. These studies show that the brackish mixing zone beneath the beachface can mitigate chemical fluxes to the ocean.

Although the aforementioned studies add to the importance of tidal and wave forcing on influencing beach groundwater flow, a comprehensive and more global understanding of the ecological function of sandy beaches cannot be achieved until the intertidal hydrologic conditions and the physical processes that act on the beach aquifer are better characterized. This thesis addresses the mechanisms that control flow beneath the beachface. To this end, the following hypotheses were developed: 1) The depth and areal extent of the circulation cell is a function of short term tidal forcing processes, tidal amplitude, and seasonal fluctuations in inland water table elevation and; 2) Seawater flux through the circulation cell is controlled by wave swash and varies across the intertidal zone and on beaches with different swash zone widths. This study incorporates various hydrologic processes including those above (e.g. wave swash and tidal undulation) and below (e.g. inland hydraulically driven flow) the beachface to determine the extent at which these processes are coupled and

their potential for altering the spatial distribution of the mixing zone over various time scales. This work builds on current understanding of beach groundwater dynamics and implements new and relatively inexpensive methodologies to investigate the physical processes that drive flow in the beach aquifer.

Chapter 2

BACKGROUND

2.1 Tide Induced Beach Circulation

In the absence of tidal and wave forcing, less dense freshwater flows on top of a denser saltwater wedge before discharging near the shoreline. In shallow beach aquifers, however, the rise and fall of sea level due to tidal oscillation will cause a permanent super-elevation of the beach water table (a rise of the water table above the elevation of mean sea level, e.g. Neilsen et al., 1990) that decays landward. The resulting increased seaward hydraulic gradient drives a saline-brackish circulation cell in the intertidal zone that overlies fresh porewater (Figure 1). This transition zone may be a region of rapid mixing between seawater and through flowing freshwater. This is supported by Michael et al., (2005), Vandenbohede and Lebbe (2005), and Robinson et al., (2006), which reveal that tidal oscillations circulate large volumes of seawater through the subterranean estuary as seawater infiltrates the upper part of the beach and exits the system at a point farther seaward. Previous authors (e.g. Michael et al., 2005 and Robinson et al., 2006) have found through field experiments and numerical simulations that circulation driven by tidal undulation contributes 3% to 80% of total SGD.

Nielsen (1990) developed an analytical solution for shore normal groundwater flow in a long straight beach with a hydrostatic pressure distribution. In a sandy homogeneous and isotropic aquifer, the groundwater flow equation can be written as the Boussinesq equation under the Dupuit assumption (Nielsen, 1990),

$$\frac{\partial h}{\partial t} = \frac{K}{n}\frac{\partial}{\partial x}\left(h\frac{\partial h}{\partial x}\right) \tag{1}$$

with the tidal oscillation dying out far inland,

$$\frac{\partial h}{\partial t} \to 0 \; as \; x \to \infty \tag{2}$$

with the tidal variation h_{tide} a function of the thickness D of the aquifer, and the slope β the beachface,

$$h([h_{tide} - D]\cot\beta, t) = h_{tide} \tag{3}$$

Although these equations offer a simple analytical solution for estimating shore-normal flow due to tides, they neglect the super-elevation of the water table above mean sea level caused by tidal inflow in the upper regions of the beachface (Turner et al. 1997). Li et al. (1999) realized that tidal oscillations drive oscillating flows and

integrated the difference between the highest water table and the average water table height to analytically approximate SGD due to tidal circulation:

$$D_t = \frac{\eta_e A}{\kappa T_t}\exp(-\alpha)\,[\cos(\alpha) - \sin(\alpha)] + \frac{\sqrt{2}\eta_e A^2}{s_b T_t}\exp(-\sqrt{2}\alpha)\cos(\sqrt{2}\alpha) + \frac{\eta_e A^2}{s_b T_t} \tag{4}$$

with

$$\kappa = \sqrt{\frac{\eta_e \omega}{2KH}} \quad , \quad \alpha = \frac{\kappa A}{s_b} \tag{5, 6}$$

where D_t is the discharge rate per unit alongshore distance, A is the tidal amplitude, T_t is the period, ω ($2\pi/T_t$) is the frequency, η_e is the effective porosity, H is the averaged aquifer thickness, and s_b is beach slope.

It is often assumed that the water table is a continuation of the tidal elevation. On a gentle sloping beachface however, an outcropping of the water table from the sea surface will take place when the rate of tidal fall exceeds the rate of water table fall (Turner et. al., 1997). This occurs because the rate at which the beach drains is less than the rate at which the tide falls. The geographic location of the intersection of the water table and the beach surface is termed the exit point. A seepage face develops seaward of this point due to the decoupling of the water table from the sea surface (Figure 2) (Horn, 2002). The seepage face typically reaches its maximum width at low tide and disappears during high tide (Li et al., 2008).

Fresh groundwater in sandy permeable aquifers is often high in dissolved nutrients originating from domestic, municipal, agricultural, and industrial practices. When this water approaches the coastline it encounters seawater to form a shallow brackish mixing zone. Since seawater is typically rich in biogenic particles (both live organisms and detritus) the conditions for denitrification (suboxic, reactive organic matter, and NO_3^-) can be met in this mixing zone. The beachface mixing zone may therefore contribute to the chemistry of the discharging fluid, with an influence that is likely dependent on the temporal and spatial dynamics of the circulation cell.

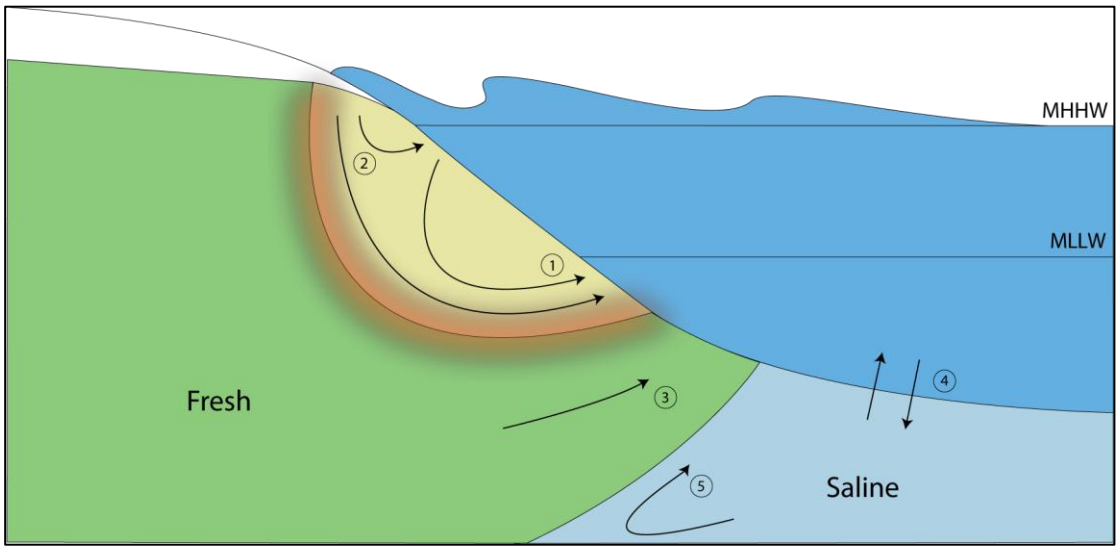

Figure 1. Mixing zone (red) and (1) Tidally induced seawater recirculation and discharge; (2) swash induced infiltration flow, and discharge; (3) Terrestrially derived fresh groundwater forcing and discharge; (4) tidal pumping resulting in fluid exchange between the saline aquifer and the surface water body and; (5) dispersive driven flow along the interface.

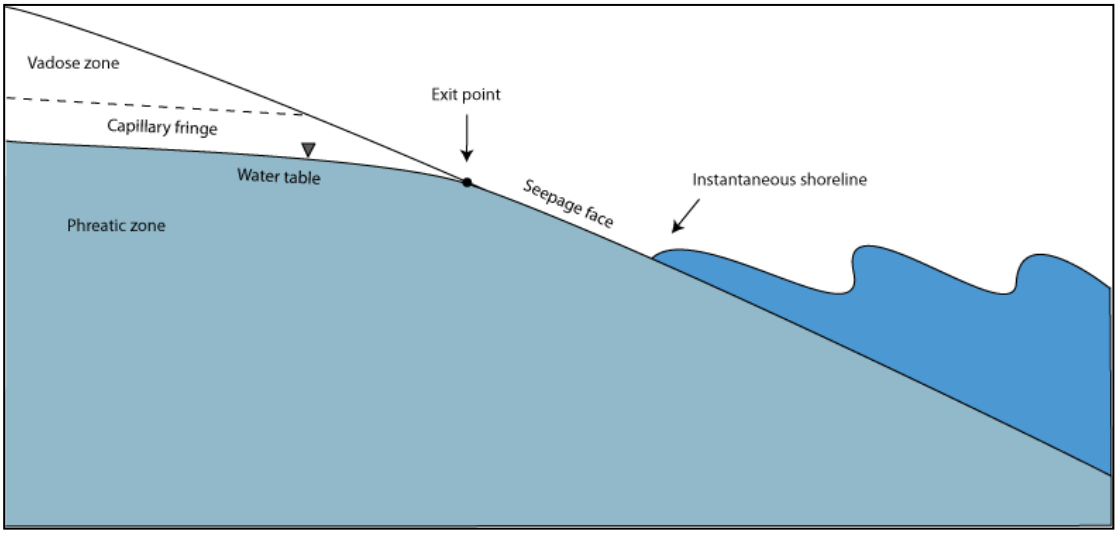

Figure 2. Decoupling of the water table from tide level.

2.2 Swash Induced Groundwater flow

The swash zone covers the region of wave run-up and run-down and therefore influences the entirely of the beachface. Previous studies on beach groundwater dynamics have addressed long term forcing mechanisms, particularly seasonal and tidal effects on water table fluctuations both within the beach and farther landward. Xin et al., (2010) recognized that few studies (e.g. Cartwright et al., 2006; Hegge and Masselink, 1991; Li et al., 2008; Li et al., 2006; Turner and Masselink, 1998; Turner and Nielsen, 1997; Riedel et al., 2010) have assessed the role of smaller scale and shorter term forcing mechanisms such as waves in controlling seawater influx across the beachface. These studies estimated infiltration-exfiltration rates by analyzing pore pressures measured by pressure sensors buried in the saturated zone, but they

neglected to account for moisture fluctuations above the water table, which are necessary to more accurately estimate swash driven influx.

Field observations (e.g. Turner and Masselink, 1998) reveal that infiltrating seawater across the beachface can be analyzed at two different time scales: 1) instantaneous flow associated with individual swash events, and 2) phase-averaged flow associated with numerous swash events that correspond to net fluid flow through the bed. Field experiments have shown swash-aquifer coupling and confirm that pore pressure responds instantaneously to individual wave overtopping, which causes vertical infiltration across the beachface and a rise of the mean water table up to 40% of the off-shore wave height above the elevation of the ocean tide (Cartwright et al., 2006; Turner et. al., 1997). Li et al. (1999) developed an analytical solution for groundwater circulation due to the phase-averaged hydraulic head gradient caused by wave swash that neglects capillarity:

$$D_w = K s_w L \tag{7}$$

with

$$s_w = \frac{3\sigma^2 s_b}{8 + 3\sigma^2} \quad , \quad L = \frac{H_b}{\sigma(s_b - s_w)} \tag{8, 9}$$

and the breaking index σ defined by Dean and Dalrymple, 1991,

$$\sigma = \frac{1.56}{1 + \exp(-19.5 s_b)} - 43.8[1 - \exp(-19 s_b)] \frac{H_b}{g T_w^2} \tag{10}$$

where D_w is the discharge rate per unit along shore distance, K is the hydraulic conductivity, s_w is the slope of the wave setup, L is the distance between the breaker line and the run-up line, σ is the breaking index, H_b is the breaker height, and s_b is the beach slope.

At the time scale of wave swash, vertical pressure gradients can be several orders of magnitude greater than horizontal gradients, forming a localized circulation cell in the vicinity of the exit point with flow into the deeper parts of the aquifer and towards the sea (Turner and Masselink, 1998). Once the swash event recedes and the exit point moves seaward, the water table begins to drop below the sand surface; initially rapidly and then at a slower rate. The rate of water table decline is a function of the distance between the swash front and the exit point (Cartwright et al., 2006). Time averaged rates of bed through-flow were observed to be two orders of magnitude greater than instantaneous fluid flow. The volume of seawater that infiltrates into the beach is limited by the volume and moisture content of the unsaturated zone, but there is no documentation of incorporating moisture content into the calculations for influx (Cartwright et al. 2006). This thesis presents new methodologies and instrumentation that takes into account moisture content and water table fluctuations when calculating flux into the subsurface.

2.3 Capillarity

The effects of capillarity can be ignored when integrating fluid fluxes over tidal frequencies; however at shorter wave swash frequencies it can affect water table dynamics and the propagation of pressure waves. Gillham (1984) demonstrated that the capillary fringe can significantly affect water exchange between the aquifer and ocean because of its ability to control the storage capacity of the aquifer when the water table is close to the land surface. Capillary effects must be taken into account in instances where influx due to wave run-up is considered because the water table is close to the beachface.

Groundwater zones are divided according to their moisture content. The zone below the water table is fully saturated and is termed the phreatic zone. Pore spaces in this zone are filled with water so pore pressures are equal to or greater than atmospheric. The vadose zone, or zone of aeration, is the unsaturated region above the water table where pore spaces are filled with both air and water and hence porewater pressure is equal to atmospheric.

Analogous to a fluid in a capillary tube, ionic attractive forces between porewater molecules and the interstitial pore space walls act to raise the water above the phreatic zone. This forms a capillary fringe, a layer between the phreatic and vadose zone that is also saturated, but with pore pressures that are less than atmospheric (Figure 2). Since pore spaces in the capillary fringe are saturated, the only identifiable characteristic that separates this zone from the phreatic zone is that pore pressures are negative (Drabsch et al., 1999).

The thickness of the capillary fringe, or tension saturated zone, can range from less than a centimeter in medium-fine sand to more than a meter in fine sediments (Jayatilaka and Gillham, 1996). Turner and Nielsen (1997) derived an analytical solution to express the thickness B of the capillary fringe in sandy beaches with cubic packing of spherical grains of uniform diameter, where the thickness is proportional to surface tension and inversely proportional to pore size and the density of the fluid;

$$B = \frac{10\sigma}{\rho g \overline{D}} \tag{11}$$

with σ empirically defined by Guohua, et al., 1994 as

$$\sigma = 75.59 - 0.13476t + 0.021352S_p - 0.00029529 \tag{12}$$

where σ surface tension (mN/m) of the fluid, ρ is fluid density, g is the gravitational field, D is the mean grain diameter, S_p is seawater density and t is the temperature of the fluid. Equation 11 was later revised by Antherton et al. (2001) to express the rise H_c of a fluid with density ρ in a capillary tube with radius R,

$$H_c = \frac{2\sigma cos\alpha}{r_m \rho g} \tag{13}$$

where σ is the surface tension, α is the angle of the meniscus within the capillary tube, r_m is the mean pore radius, and g is the gravitational field.

2.4 Regional Setting

Cape Henlopen is a sandy beach spit located on the Delmarva Peninsula along the mid-Atlantic coast of the United States (Figure 3a). It forms the southern boundary of the Delaware Estuary and lies approximately 3 km east of Lewes, Delaware and 6 km north of Rehoboth Beach, Delaware. Cape Henlopen experiences erosion along its Atlantic boundary and deposition behind the spit (Miller and Ullman, 2004). These two processes are responsible for a northward propagation of the spit of approximately 2.4 km in the last 160 years (Ramsey & Wang, 2001). A series of beach dunes, berms, and ridges comprise the spit and are associated with the Pleistocene and Holocene evolutional history of The Cape (Kraft et al., 1971)

2.5 Study Area

Field measurements of subsurface salinity, porewater pressure, and soil moisture content were obtained from two microtidal sandy beaches at Cape Henlopen (Figure 3b). Experiments were carried out on Cape Shores, a tide dominated sandy beach located on the bay side of The Cape (Figure 3c). The mean grain size (512 µm) was calculated from a cumulative plot of grain size using standard sieving procedures (Folk, 1974). A series of offshore bars exposed during spring low tides made this site well suited for offshore porewater sampling. Salinities in the estuarine water column

are influenced by the freshwater discharge of the Delaware River and range from 27-30‰ throughout the year (Kawabe et al., 1988; Sharp et. al., 1982). A secondary field site, Herring Point, was established to study effects of swash zone width on swash-induced infiltration (Figure 3d). This high-energy wave-dominated beach is located along the Atlantic coastline on the opposite side of the spit (Figure 3d) and is subjected to larger amplitude waves that can produce a swash zone that is in excess of 10 m wide compared to 1 m at Cape Shores while maintaining a similar tidal range (1.2 m). Mean low water (MLW) for Cape Shores and Herring Point is -0.75 m relative to the North American Vertical Datum of 1988 (NAVD 88) and mean high water (MHW) for both study areas is 0.49 m relative to NAVD 88. MSL (mean sea level) for both study sites is -0.12 m relative to NAVD 88. Salinities offshore of Herring Point range from 33-35‰ throughout the year. Cape Shores offshore wave height is <1 m, with a median wave height of 25cm measured on 10/08/2009. The Herring Point offshore wave height is 1.95 m (USACE 1996, 1997).

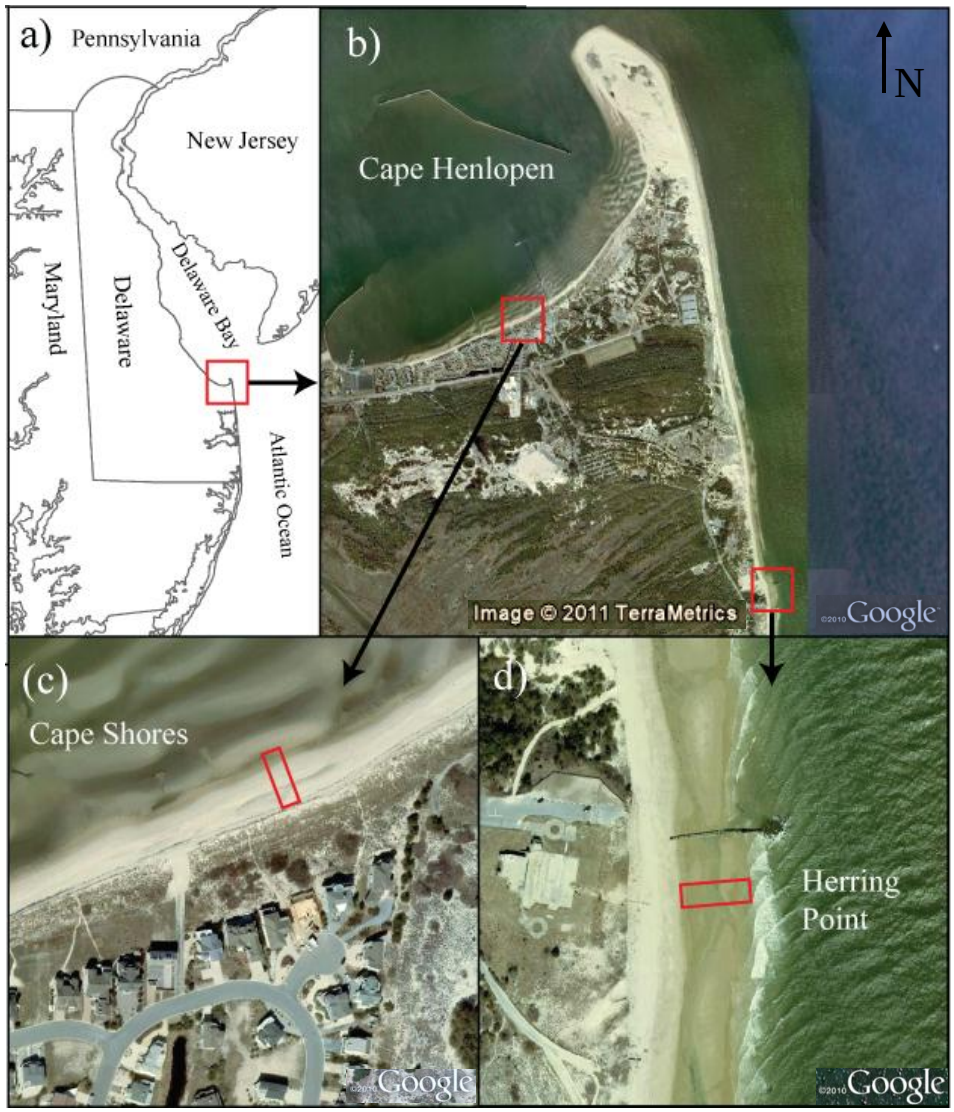

Figure 3. Location of Cape Henlopen field sites: (a) Delmarva Peninsula and Delaware Bay; (b) Cape Henlopen at mouth of Delaware Estuary; (c) Low energy Cape Shores site at Breakwater Harbor; (d) High energy Herring Point site along Atlantic Ocean.

Chapter 3

METHODS

3.1 Instrumentation

Two measurement strategies were implemented to examine groundwater-seawater interaction in the beach. Multilevel samplers installed at Cape Shores were used to sample porewater at regular vertical and horizontal intervals over a range of time scales. The second measurement strategy utilized two types of high frequency probes buried in the beach. Pressure transducers were installed in order to capture rapid head fluctuations due to wave swash while moisture sensors located in the unsaturated zone monitored the effects of wave swash on moisture content. Time series generated by both sensor types were used to describe the vertical seawater influx across the beachface on the time scale of wave swash at mean lower low water (MLLW) and mean higher high water (MHHW) the Cape Shores and Herring Point study sites.

3.2 Multilevel Porewater Samplers and Installation

Multilevel porewater samplers were constructed from 2.5 cm OD PVC pipe and three to five sections of 0.64 cm diameter polyethylene tubing. Each section of tubing was fastened to the outside of the PVC pipe and outfitted with a 3 cm nylon

mesh screen at one end (Figure A2). The samplers were installed in shore-perpendicular transects between the dune line and the first offshore bar to a maximum depth of 3.5 m (Figure 4) by hand augering through a PVC casing, which was removed to allow the borehole to backfill once the samplers were in place. Since the infilling of the borehole disrupted the adjacent porewaters, the sediment and groundwater flow was allowed to equilibrate one week before sampling began. These instruments were used to sample porewater for salinity measurements at tidal to seasonal time scales. Due to decreased wave energy during the summer months compared to winter, there was a net transport of sand onshore that raised the beach profile and a net transport offshore during the winter that lowered the profile up to 0.5 m (Figure 4). The beachface elevation during the winter was eroded to a point where the three samplers closest to the dune line were lost and had to be later reinstalled. It was determined by standard surveying techniques that the locations of the new sampling ports were within 0.5 m of their original location (Figure 4). The positions of the summer sampling ports were referenced to the stratigraphic cross-section that was obtained by hand augering to a depth of about 3 m at four locations perpendicular to the shoreline (Figure 5). The vertical positioning of the sampling ports were referenced to NAVD 88 from a Coast and Geodetic Survey marker (Designation 855 7380 Tidal 40) approximately 270 m from the study area using standard surveying procedures. Sea surface levels were measured from a tidal gauging station located 1 km west of the study area (NOS Station 8557380, Lewes, DE) and corrected to NAVD 88. Twenty-three porewater samples were collected per sample run along the transect

beginning with the ports located 27 m from the benchmark and ending with the offshore ports located 56 m from the benchmark when the minimum tidal level was -0.18 m below MLLW as measured by the Lewes gauging station. Groundwater was extracted from the sampling ports using a peristaltic pump and salinity was estimated using electrical conductivity measurements.

The multilevel samplers were installed with the objective of characterizing the geometry of the salinity mixing zone over time scales ranging from hours to months. This addressed Hypothesis 1, as the shorter sampling intervals were intended to capture snapshots of subsurface salinity at various stages in the tidal cycle, highlighting the response of the aquifer to tidal forcing. Longer term measurements of porewater salinity using the samplers tested the seasonal aspect of Hypothesis 1

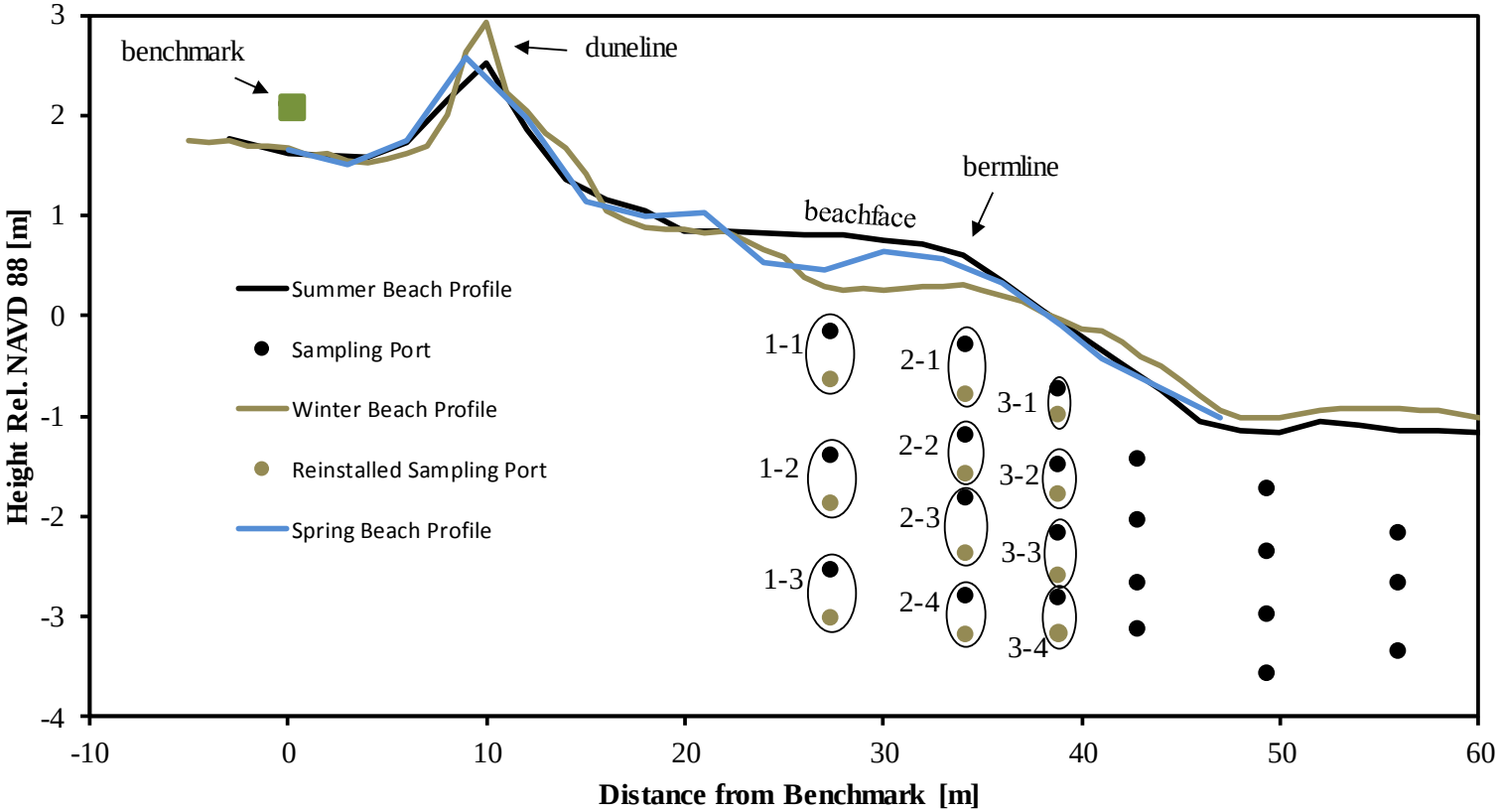

Figure 4. Seasonal beach profiles at Cape Shores. Offset between black and gold symbols indicate difference in vertical positioning between summer and winter sampling ports.

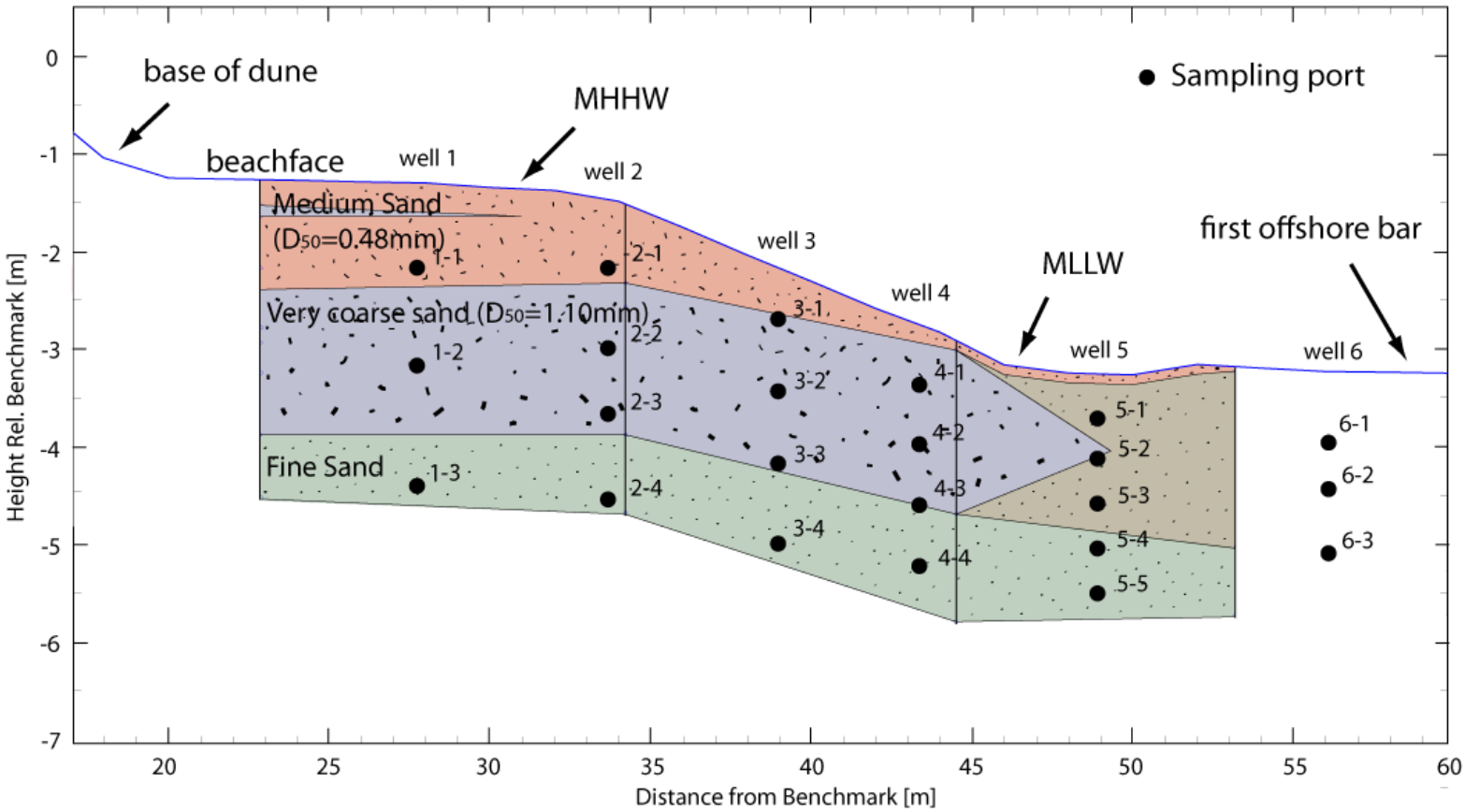

Figure 5. Cape Shores cross-sectional view of vertical and horizontal distribution of sampling ports and beachface stratigraphy as determined by hand augering. Vertical black lines indicate the location where auger cuttings were collected.

3.3 Sensors

3.3.1 Pressure Transducers and Calibration

Four GE Druck PTX 1835 vented pressure sensors buried directly in the beach recorded high frequency pore pressure fluctuations and hydraulic gradient variations due to wave swash. These instruments contain a silicon piezoresistive pressure sensor with a maximum accuracy of ±0.1% for any pressure range between 5 and 900 psi. The default factory calibration assigned each sensor identical calibration equations, however minor inconsistencies in diaphragm fabrication may have resulted in sensors that were slightly more or less sensitive to input compared to other sensors. In order to ensure the highest attainable accuracy, the transducers were individually recalibrated in the laboratory and assigned their respective calibration curve. For this procedure, each sensor was submerged under a known depth of water and the millivolt output was plotted as a function of depth (Figure 6). The linear correlation coefficient for all sensors is extremely close to one, indicating the sensors can be used to precisely define the pressure field. The excellent accuracy and precision of these instruments is necessary to resolve small (< 2 cm) head fluctuations over relatively short (50 cm) horizontal distances.

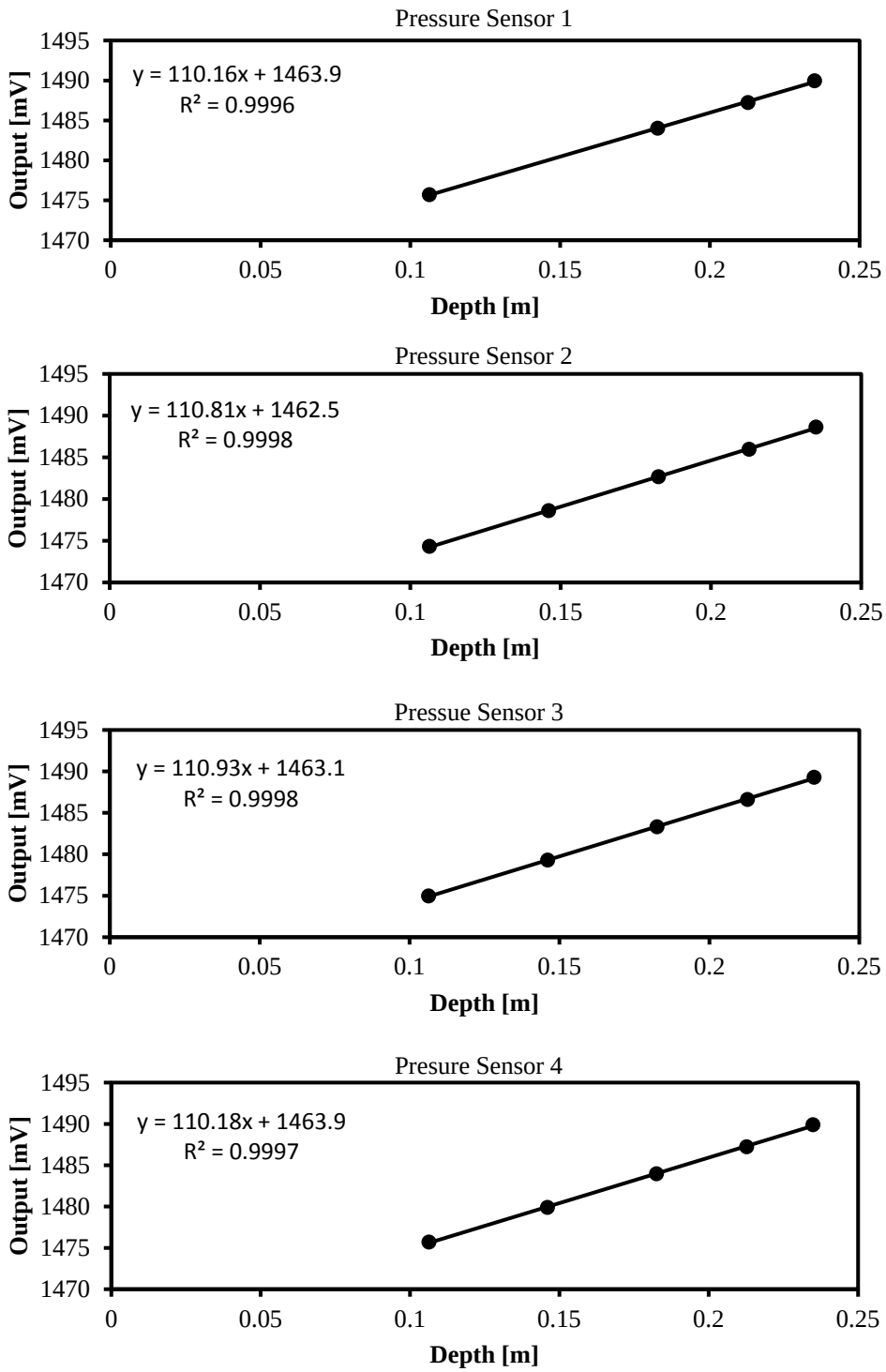

Figure 6. Pressure sensor millivolt output as a function of water depth.

3.3.2 Moisture Sensors and Calibration

Presence of the capillary fringe underscores the importance of co-locating pressure sensors and moisture sensors in order to distinguish between apparent and real moisture fluxes in shallow water table environments. When the upper extent of the capillary fringe is within one-half the average grain diameter from the sediment surface, the addition of a disproportionately small amount of water will cause the head to fluctuate up to the thickness of the capillary fringe. In this special case shallow water table situation, the specific yield of the saturated sediment above the water table is close to zero. This phenomenon is known as the reverse Wieringermeer effect and has important implications in calculating moisture exchange rates and reducing the aquifer storage coefficient because the pressure fluctuations below the water table cannot be attributed to a loss (or gain) of moisture equivalent to the thickness of the capillary fringe (Cartwright et al., 2006).

Direct measurement of moisture content in the swash zone is important for two reasons. First, the moisture sensors record in-situ volumetric water content which takes into account sediment porosity. Secondly, since the moisture measurements do not depend on pore pressure, the error related to the disproportionate rise and fall of the water table associated with a minor input or removal of water from the system (i.e. reverse Wieringermeer effect) is removed from the calculations. This approach takes into account the moisture content of the unsaturated zone in order to prevent overestimating influx, which would occur due to large pressure fluctuations.

Twelve Decagon EC-5 Soil Moisture sensors were used to monitor the effects of wave swash on soil moisture content. The depth to the water table in the swash zone is shallow, so these sensors were chosen for the small volume of soil needed to obtain a volumetric water content measurement, defined as the volume of water per unit volume of bulk sand. The probes measure the dielectric constant of the soil, which is a function of water content, salinity, and soil texture. Variation in soil texture and salinity can result in approximately ±3-4% accuracy for most medium to fine textured sediments and up to ±10% for coarse grained and highly saline sediments. For best results, a soil specific calibration was conducted in order to increase accuracy to ±1-2%. The experimental volumetric water content was determined by standard gravimetric analysis and was plotted as a function of probe mV output in order to obtain the calibration curve (Figure 7). A calibration curve was generated for both study sites using sediment samples and seawater obtained from each site. The resolution, precision, and repeatability of the sensors are excellent, so the calibration of one sensor was applied to all other moisture sensors. The following procedure was used to calibrate the Decagon EC-5 Soil Moisture probes for soil and salinity.

1) A sand sample from the approximate location of sensor deployment was air dried in the laboratory
2) Large rocks, shells, and organic debris were removed as these materials tend to make the porosity of the sand matrix heterogeneous
3) Large aggregates of sand were broken into their individual grains using a mortar and pestle.

4) A portion of the sample was packed into a 500mL calibration chamber in layers to ensure that the bulk density was near the field bulk density.

5) The probe was inserted vertically into the center of the container such that only the wire was protruding from the sand surface.

6) The probe mV output was recorded.

7) A small volumetric soil sample was obtained from undisturbed sand adjacent to the probe.

8) The mass of the small sand sample was recorded.

9) Approximately 250mL of seawater from the field site was mixed into the original sand sample.

10) Steps 4 through 9 were repeated until the soil reached saturation.

11) The mass of each volumetric soil sample was recorded after they dried at 45.5 degrees Celsius for 24 hours.

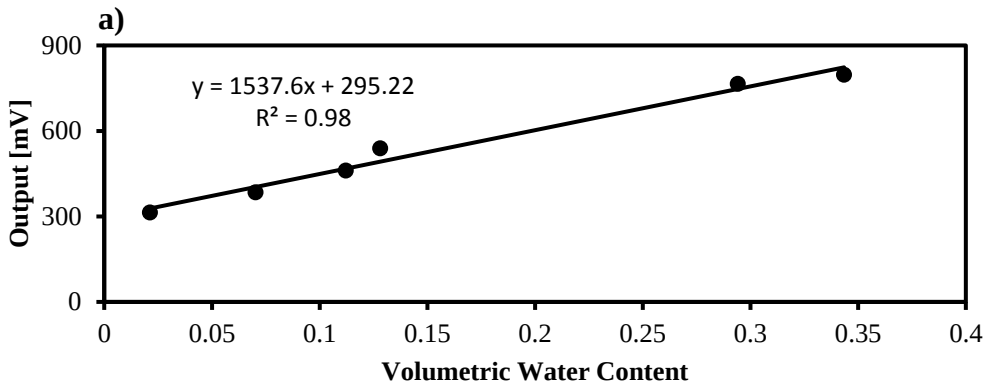

Figure 7. Moisture sensor millivolt output as a function of volumetric water content. a) Cape Shores site and; b) Herring Point site.

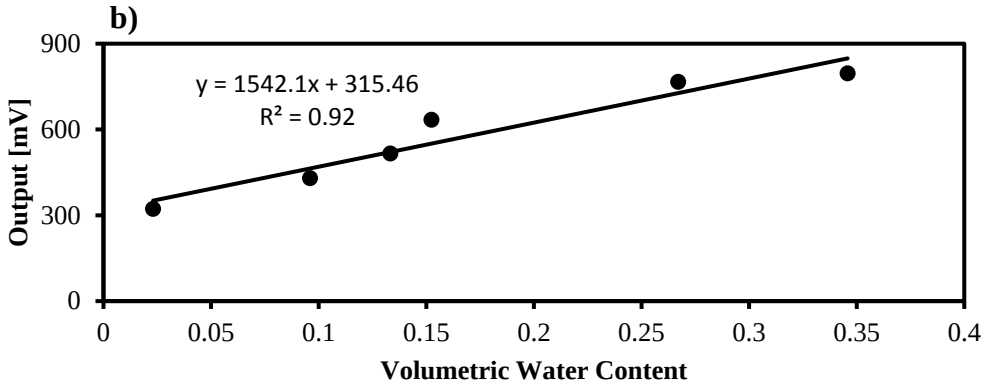

Figure 7. Continued.

3.3.3 Sensor Deployment

Pressure sensors and moisture sensors were installed in the beach subsurface to investigate the saturated and unsaturated behavior of the swash zone as it tracked up the beachface. Prior to installation, the pressure transducers were outfitted with a nylon screen over the pressure port in order to eliminate the mechanical force of sand grains colliding with the diaphragm. Each pressure sensor was fastened vertically to the end of a wooden dowel after the void space between the diaphragm and the nylon screen was filled with seawater to purge air bubbles. Three moisture sensors were secured perpendicular to each dowel so that the metal rods used to integrate the volumetric water content were parallel to the water table and infiltrating seawater (Figure 8). This allowed the sensors to be spaced closer together without interference between their electromagnetic fields and allowed them to be inserted horizontally into undisturbed sand for high vertical resolution. The depth to the water table increases with distance from the shoreline, so the vertical separation between the moisture sensors was adjusted so that they were equally distributed in the unsaturated zone. The

dowels were installed by hand auguring in shore-perpendicular transects. Once the desired depth was reached, the dowels were inserted such that the pressure sensors were positioned below the water table where they remained for the duration of the experiment (Figure 8). The moisture sensor prongs were pushed into the undisturbed soil of the borehole wall to ensure that the sensors were measuring the volumetric water content at the approximate bulk density of the subsurface. The borehole was then backfilled overtop the sensors to the field bulk density. Burial of the pressure sensors directly in the sand matrix eliminates frequency response issues associated with conventional piezometers (Turner and Neilsen, 1997).

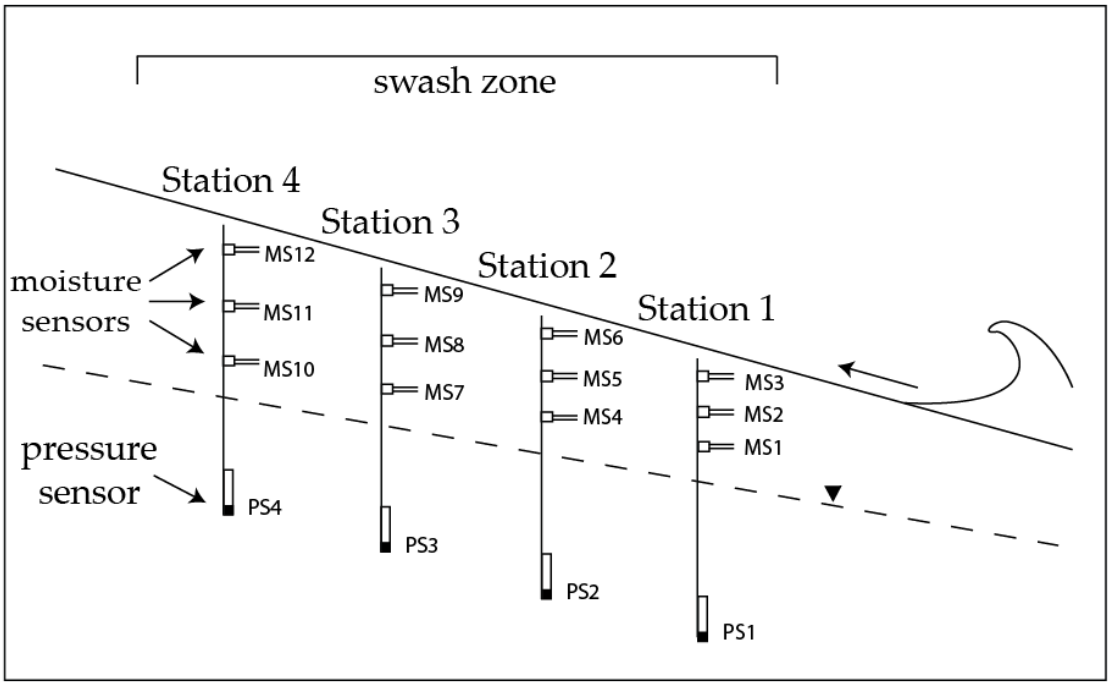

Figure 8. Cross-sectional view of instrumentation in the swash zone.

In order to integrate influx rates across the beachface, four experiments were conducted near MHHW and MLLW at the Cape Shores and Herring Point study sites. Figure 9 shows a map view of the MHHW deployment scheme and Table 1 highlights the time and duration of each sensor experiment. Verified tide elevations to two days prior to each experiment can be found in Appendix C.

Table 1. Time and duration of sensor experiments

Location	Date	Beachface Position	Start Time	End Time	Runtime [minutes]
Cape Shores	1/19/2011	MLLW	2:09PM	4:52PM	163
Cape Shores	4/14/2011	MHHW	4:31PM	7:30PM	179
Herring Point	3/18/2011	MLLW	2:12PM	6:00PM	228
Herring Point	4/25/2011	MHHW	4:50PM	7:17PM	147

For each of the four experiments, the instruments were installed prior to high (or low) tide. In order to ensure that the sand matrix surrounding the sensors became fully saturated by the end of each experiment, and to encompass the entirety of the swash zone, the positioning and horizontal interval between each station was based on the maximum wave run-up distance. By measuring the width of the swash zone and by testing various sensor configurations, the spacing was set to 0.5 m for the Cape Shores site and 1.0 m for the Herring Point site. All sensors were cabled to a Campbell Scientific CR1000 datalogger and logged synchronously at 5 Hz. To minimize the amount of seawater that tended to collect around the wiring, the cables were buried in a trench leading up the beachface to the data acquisition system. Time series'

generated by both sensor types were used to describe vertical seawater influx across the beachface on the time scale of wave swash. The use and configuration of the moisture sensors will address Hypothesis 2 by monitoring fluctuations in moisture content (allowing calculation of fluid flux) through the unsaturated zone.

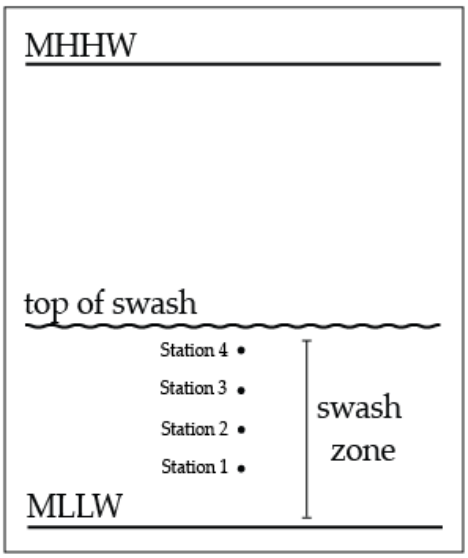

Figure 9. Map view of sensor deployment near MLLW. Not to scale.

3.4 Signal Processing

Infiltration rates due to wave swash were calculated near the mean low and mean high water levels at both field sites. A five-point unweighted moving average was applied to each moisture sensor time series in order to remove random noise while maintaining sharp step response in the output signal. The five-point moving average was chosen because the smoothing action and the decrease in amplitude of the output signal was minimal compared to the decrease in random noise. Although a larger moving average could have been used to further attenuate noise, it was deemed that a

larger value would have dampened the signal to a point where the filtered data was a poor representation of the actual moisture response. Equation 14 shows the frequency response of the moving average filter:

$$H[f] = \frac{\sin(\pi f M)}{M\ sin(fM)} \tag{14}$$

where M is the number of moving average points and f is the frequency. It is evident that the moving average cannot differentiate between one band of frequencies from another. Therefore its poor performance in the frequency domain is sacrificed for good performance in the time domain. The moving average was implemented because it effectively operates as a simple low-pass filter that attenuates high frequency, low amplitude fluctuations while preserving larger amplitudes at lower frequencies. Since the amount of noise reduction is equivalent to the square-root of the number of points, the five point moving average reduced the noise by a factor of 2.24.

A seven order low-pass Butterworth filter (Butterworth, 1930) with a normalized cutoff frequency of 0.01 was used on each moisture sensor time series to further remove noise and isolate volumetric moisture content fluctuations due solely to wave swash. As seen in Figure 10a, this type of signal processing provides a very close approximation to the unrestricted signal because of its ability to preserve specific frequencies as specified by the user, in this case 0.01. Peaks and troughs (Figure 10b) were then isolated and the difference in moisture content between consecutive peaks

and troughs for each sensor was summed over the full time domain (Figure 10c) and multiplied by the area around the sensor that was assumed to experience the same moisture fluctuations as those of the nearest sensor. Although this assumption only yields an approximation by interpolating moisture content, it was deemed that the number of sensors was adequate to estimate moisture content throughout the unsaturated zone because of the relative homogeneity of the sand matrix. The equations used to define the area of Moisture Sensor 1 (A_{ms1}), A_{ms2}, and A_{ms3} are presented;

$$A_{ms1} = (Depth_{ms1} + (Depth_{ms1} - \frac{1}{2}(Depth_{ms1} + Depth_{ms2})) - \frac{1}{2}(Depth_{ms1} + Depth_{ms2})) * 100d \quad (15)$$

$$A_{ms2} = (\frac{1}{2}(Depth_{ms1} + Depth_{ms2}) - \frac{1}{2}(Depth_{ms2} + Depth_{ms3})) * 100d \quad (16)$$

$$A_{ms3} = \frac{1}{2}(Depth_{ms2} + Depth_{ms3}) * 100d \quad (17)$$

where d is the horizontal distance between sensors and $Depth_{msx}$ is the sensor depth below the sand surface. Areas for MS4-MS6, MS7-MS9, and MS10-MS12 (Figure 11) were calculated using this same technique. Figure 11 illustrates the relative size and distribution of the cells and their corresponding moisture sensor. The moisture content change for all cells over the full time domain was then summed and divided by the

distance between the farthest seaward and farthest landward sensors to yield the depth [m] of seawater that infiltrated into the beach over the duration of the experiment. Assumptions associated with these calculations are discussed in Section 5.3.

Pressure sensors buried in the swash zone beneath the water table were used to measure rapid hydraulic gradient fluctuations due to individual swash events. Pore pressures were referenced to an arbitrary vertical datum by measuring the slope of the beachface between each station. The slopes were used to estimate the change in elevation of the sand surface over the horizontal distance between each sensor. In order to calculate the hydraulic gradient between each station, the beach slope, sensor depth, and saturated pore pressure was used to reference the position of the water table to the arbitrary vertical datum.

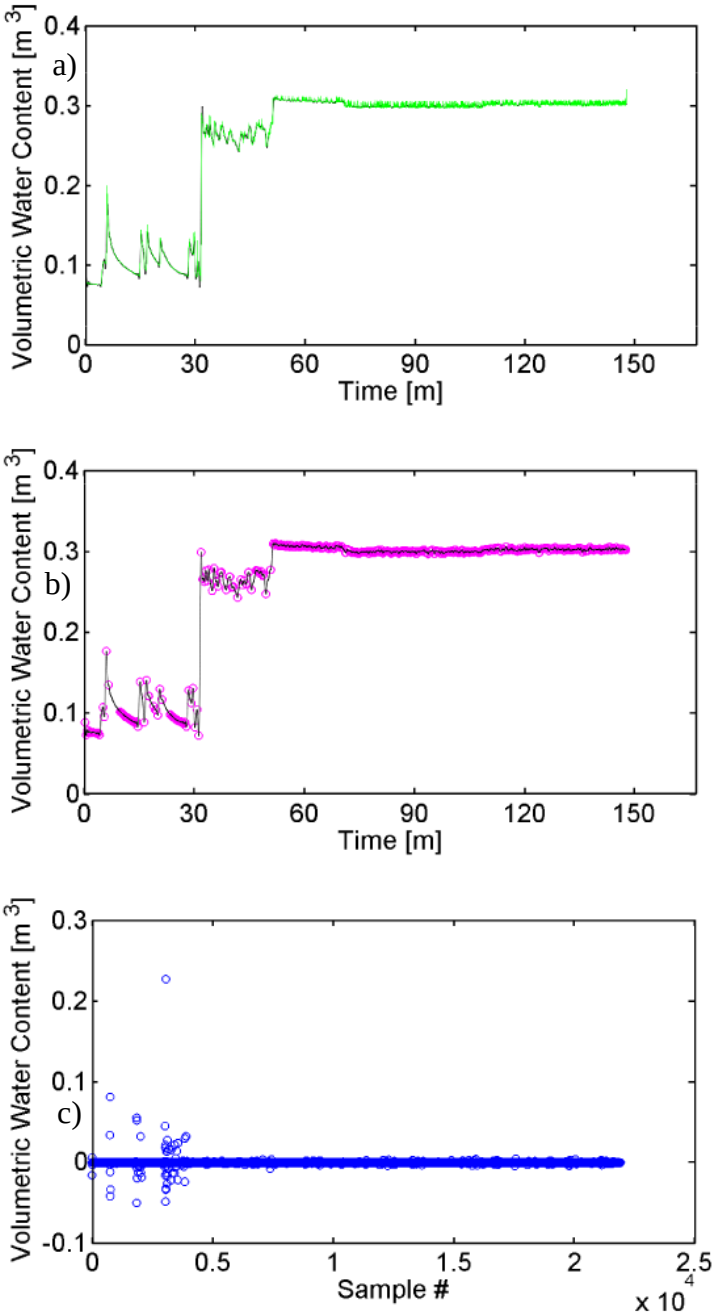

Figure 10. MS12 time series. The time domain is the full length of the experiment. a) Butterworth filter (black) applied to raw data (green); b) isolation of peaks and troughs in filtered data; c) change in moisture content between consecutive peaks and troughs.

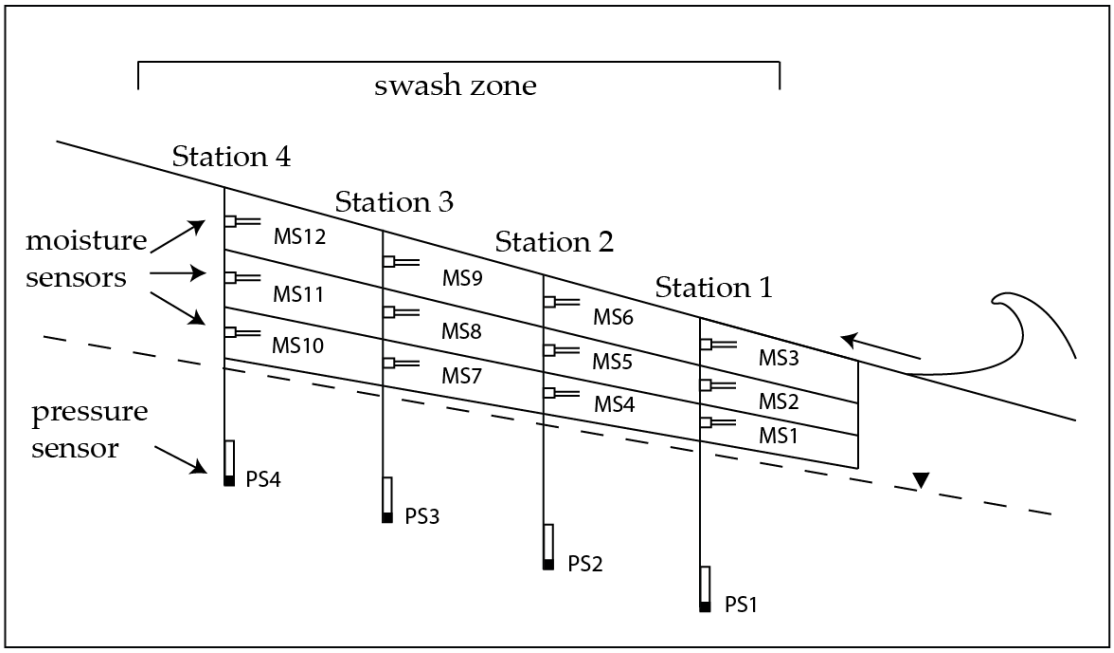

Figure 11. Areas assumed to experience similar moisture fluctuations equivalent to the nearest moisture sensor.

Chapter 4

RESULTS

4.1 Intertidal Saltwater Circulation

In order to quantitatively characterize the role of the beachface in biogeochemical cycling, the physical dimensions and the changes in the size and shape of the circulation cell over time scales ranging from less than an hour to months must first be characterized. Here, cross sections of subsurface salinity obtained over a tidal cycle, a spring-neap cycle, and a seasonal cycle are presented. These profiles will help identify the hydrologic processes that contribute to the cell's formation. Swash induced infiltration at both study sites is also presented. To aid in data interpretation, tide elevation data two days leading up to each sampling event and sensor experiment can be found in Appendix C and daily precipitation totals ten days before porewater sampling can be found in Appendix D.

4.1.1 Tidal Cycle Influences

Figure 12 shows a time series of subsurface salinity distribution over a tidal cycle on September 10, 2010 at Cape Shores with corresponding sampling events in Figure 13. There appears to be no correlation between cell geometry and daily precipitation. Porewater samples indicate that a well-developed brackish-saline

circulation cell extended approximately 32 m to 45 m from the benchmark with a minimum elevation of -3.0 m relative to NAVD 88 (Figure 12). Porewater salinities decreased with increasing depth and reached the lowest levels (1-5‰) beneath Well 1. The highest salt concentrations were found in the shallow depths beneath the beachface (25-29‰) near mean low tide.

Salinity throughout the aquifer was highest during high tide, with the brackish zone extending farthest landward and reaching its greatest depth beneath the middle of the beachface during this stage in the tidal cycle. Concentrations in the upper sediments were the same as those found in the bay (29‰). As the tide receded to a point below the mean tide level, salinity decreased only slightly. This is marked by a decrease in the cross sectional area of the cell and a shift of the mixing zone toward the surface. Salinities continued to decline with sea level as low tide approached. Offshore porewater collected during low tide revealed that the circulation cell extended to a depth of slightly over 4 m (Figure 12c) and was met with a brackish (5-8‰) discharging plume 44-50 m from the benchmark. The question mark located on Figure 12 on the Low Tide cross section highlights the unreliability of the interpolation algorithm used to approximate salinities between sample ports. This marker points to an artifact that suggests that salinity increased by 2‰ between port 5-1 and the surface. It should be noted that the salinity of the discharging porewater in this region cannot be determined from these data. Farther seaward, the position of the assumed Ghyben-Herzberg interface can be identified by higher salinities between 52 m and 56 m from the benchmark. Subsurface salinity throughout the aquifer was

lowest during the onset of flood tide approximately 2-3 h following low tide. Aquifer salinity at this tidal stage was significantly lower than during high tide. Salinity increased midway through flood tide as the water level inundated the lower and middle sections of the beachface.

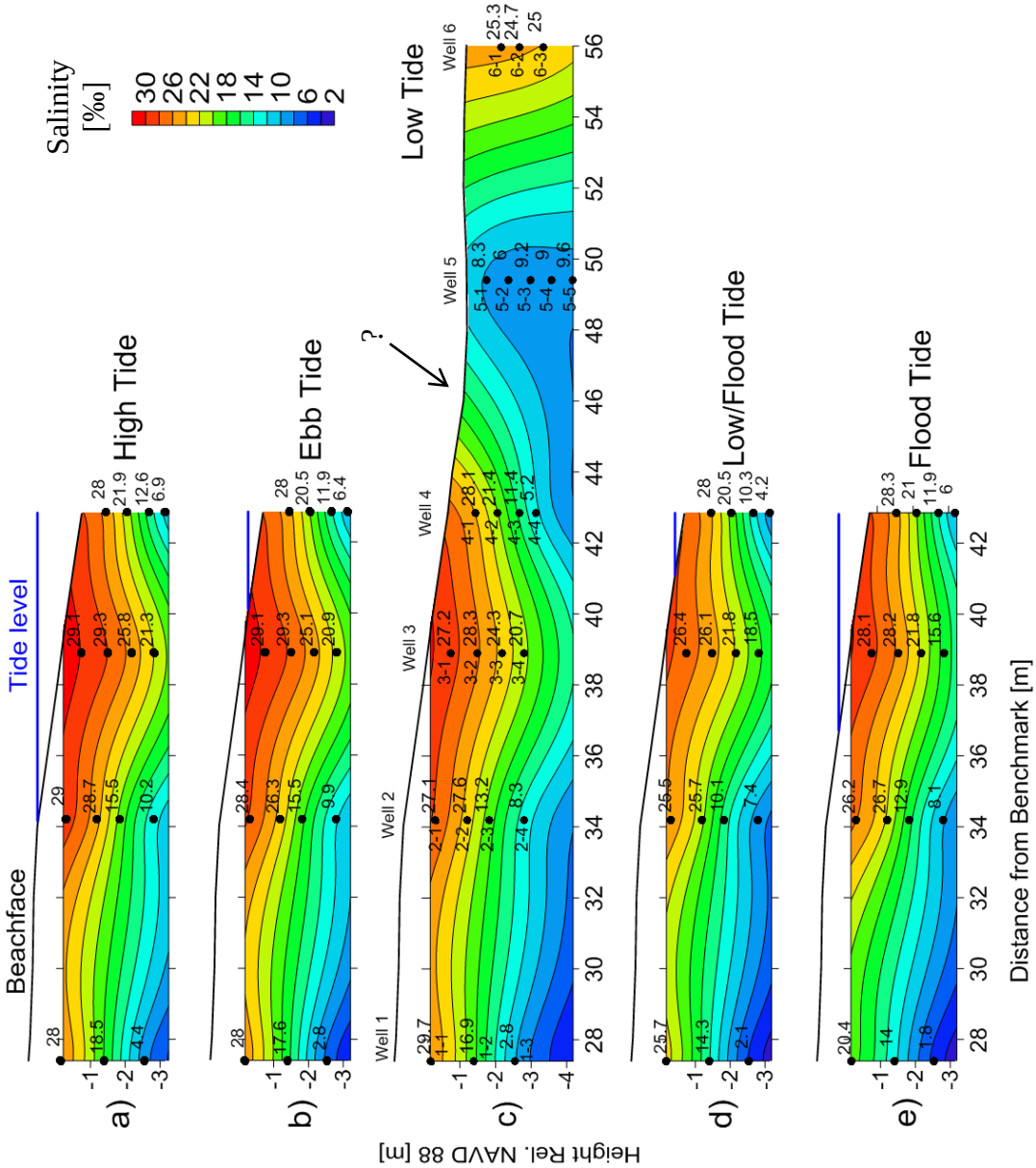

Figure 12. Time series of cross-sectional subsurface salinity distribution over a tidal cycle at Cape Shores on September 10, 2010. Porewater sampling began near high tide and continued approximately every two hours until the onset of the following high tide. Sample runs lasted approximately thirty minutes, so profiles effectively represent snapshots of porewater salinity. Water level is below sand flat elevation in Figure 12c, so it is not shown. Bay water salinity during the sampling events was 29‰. Tide elevation data from Lewes, DE (NOS # 8557380) tidal gauge station.

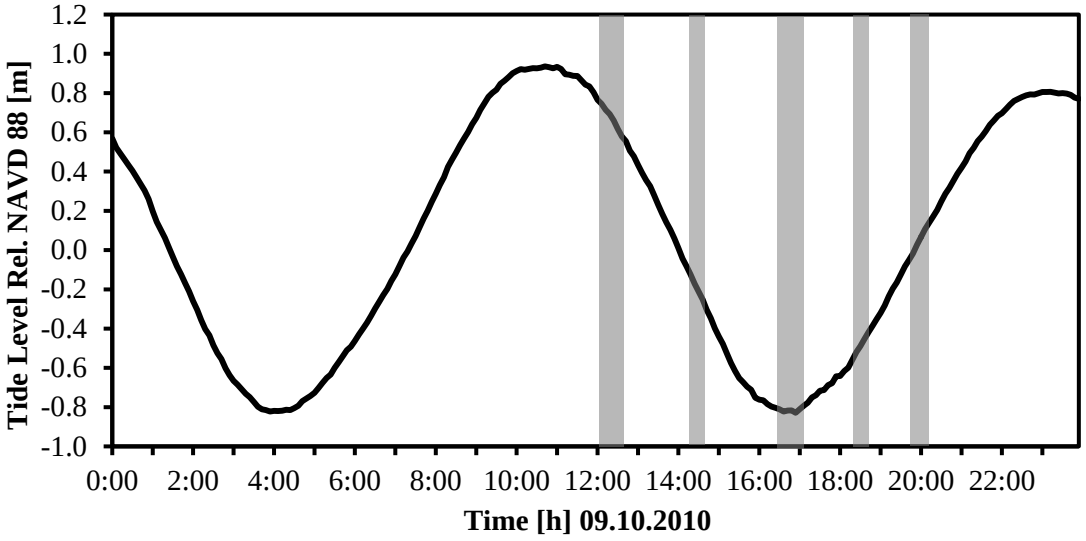

Figure 13. Sample interval during September 10, 2010 field experiment. The gray bars show the time and duration of each sample run. Sampling began at the onset of ebb tide and continued consecutively until midway through flood tide.

A similar time series obtained in August 11, 2010 (Figure 14) also indicated the presence of a density inversion that closely resembled the pattern seen in the September 10, 2010 cross sections. Porewater salinities confirmed that this aquifer responds to tidal forcing. Unlike the September 10, 2010 time series, salinities measured nearest high tide were not the highest observed concentrations over the course of the experiment. Salinities in the shallow (0-1.75 m) sediments seaward of 34 m increased 2-3‰ from high tide to the middle of ebb tide while intruding freshwater in the deeper parts of the aquifer decreased salinities in all other regions of the aquifer, forming a strong vertical concentration gradient (Figure 14a-b). Comparison between the High Tide and Ebb Tide profiles (Figure 14a-b) landward of 34 m also reveals an increased horizontal density gradient as salinities beneath Well 1 remained relatively

fresh while shallow and seaward porewate increased in salinity. Offshore porewater (Figure 14d) suggests an absence of a freshwater discharge zone between 42.4 m and 56 m, however the low tide profile from September 2010 proves otherwise. Well 5 in the September 2010 experiment (Figure 14c) indicates the presence of the freshwater discharge zone. Porewater throughout the aquifer remained relatively stable from Ebb/Low Tide to Low Tide (Figure 14c-d). The lowest dissolved salt concentrations were observed approximately three hours after low tide during flood tide (Figure 14e). Salinities at a depth from 0 m and 1.75 m between 34 m and 43 m from the benchmark ranged from 4.1‰ to 25.5‰, the smallest range observed during the experiment (Figure 14e). Porewater salinities in the Flood Tide and Flood/High Tide cross sections (Figure 14e-f) between 28 m and 30 m from the benchmark indicated the presence of a brackish wedge that extended inland. The encroachment of this brackish water was likely due to the higher hydraulic conductivity associated with the sediment found at this depth, however this phenomena was not observed during the September sampling events. The rise in salinity in the Flood/High Tide cross section (Figure 14f) was consistent with the increase in salinity during flood tide in the September 2010 time series (Figure 12e). Subsurface salinities during Flood/High Tide in the upper sediments of the intertidal zone ranged from 24-26‰ and from 16-18‰ in the bottom regions of the aquifer. An increase in salinity seaward of 31 m from the benchmark was accompanied by a slight decrease in porewater salinity between 27.4 m and 31.0 m from the benchmark. Once salt concentrations began decreasing beneath the intertidal zone during Ebb Tide, there was an increase in salt content in Well 1. As

salinities began increasing seaward of the berm line, concentrations between 27.4 m and 30 m decreased, reaching a minimum of 4-1‰ near high tide. The 2-3 h lag between high tide and highest measured salt concentrations beneath the intertidal zone is evident in both the August and September cross-sections.

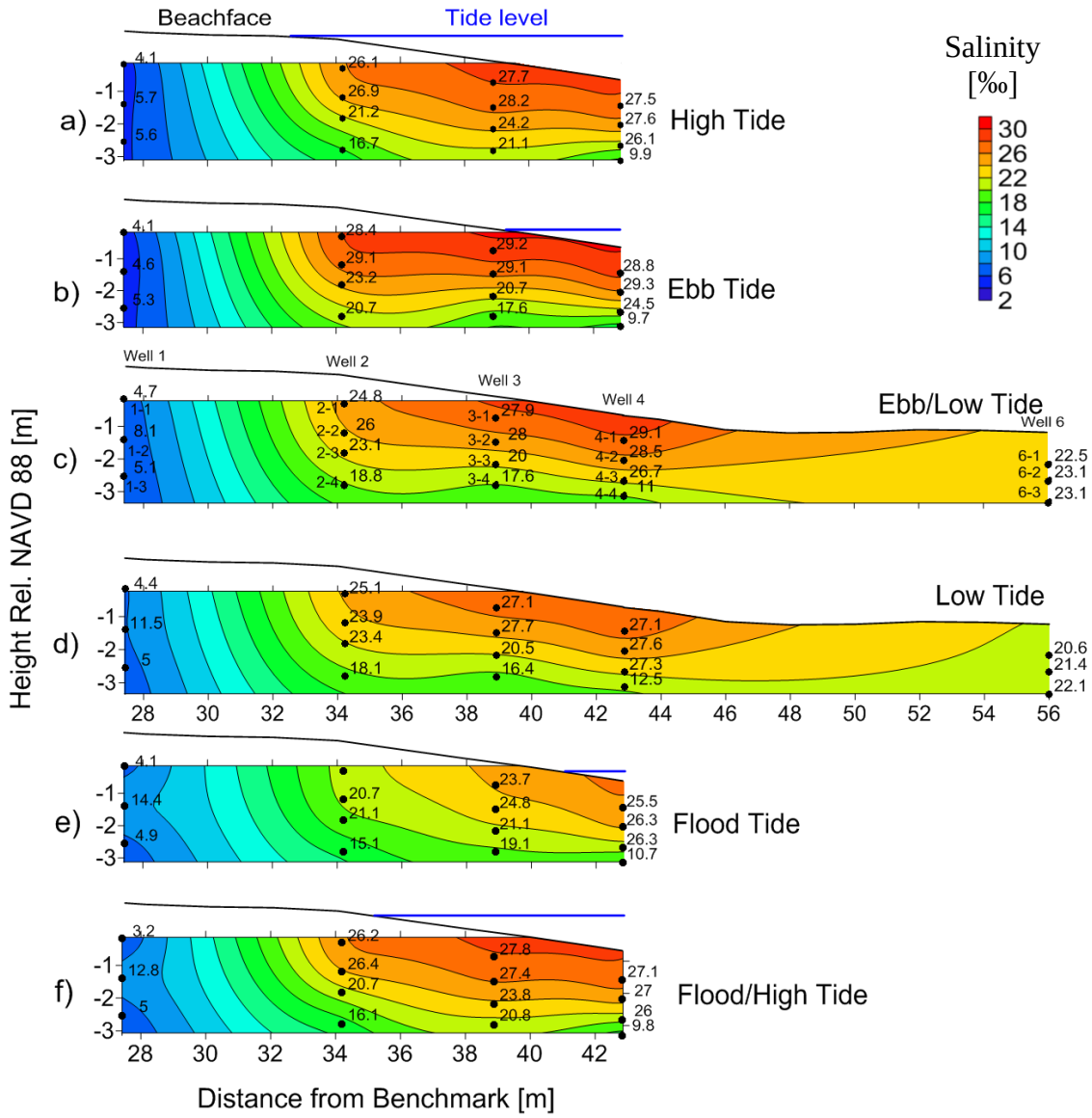

Figure 14. Time series of cross-sectional subsurface salinity distribution over a tidal cycle at Cape Shores on August 11, 2010. Porewater sampling began near high tide and continued approximately every two hours until the onset of the following high tide. Sample runs lasted approximately thirty minutes, so profiles effectively represent snapshots of porewater salinity. Water level is below sand flat elevation in Figure 14c, so it is not shown. Bay water salinity during the sampling events was 29‰. Tide data from Lewes, DE (NOS # 8557380) tidal gauge station.

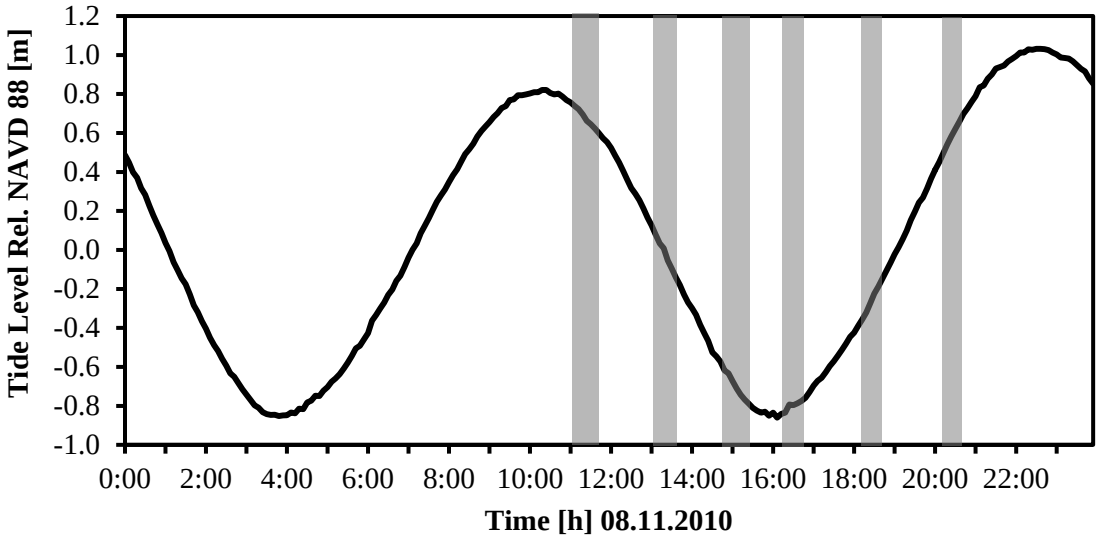

Figure 15. Sample interval during August 11, 2010 field experiment. The gray bars show the time and duration of each sample run. Sampling began at the onset of ebb tide and continued consecutively until near the end of flood tide.

4.1.2 Tidal Amplitude Influences

Salinity distribution, depth, and areal coverage of the circulation cell were also shown to be a function of tidal amplitude as shown in Figure 16. Figure 17 illustrates the difference in tidal amplitude between the two sampling dates. Both sampling events were performed near high tide as shown in Figure 17. The larger tidal amplitude associated with the September neap tide caused the circulation cell to extend 5 m farther inland compared to the smaller tidal amplitude associated with the October neap tide (Figure 16a-b). The larger amplitude during spring tide caused the mixing zone to expand horizontally as the tide level rose to the higher elevations of the beachface. Note that the tide elevation during spring and neap sampling was very near the same level in order to reduce the influence of tidal cycle effects as indicated above.

The difference in geometry could be the result of seasonal changes in upland water table elevation given that subsurface salinity used to represent neap tide aquifer conditions was acquired three weeks after the spring tide experiment; however Figure 19 indicates that there was no significant change in inland water table elevation between 09/11/2010 and 10/01/2010. This suggests that the variation between salt concentrations were primarily due to the difference in tidal amplitude.

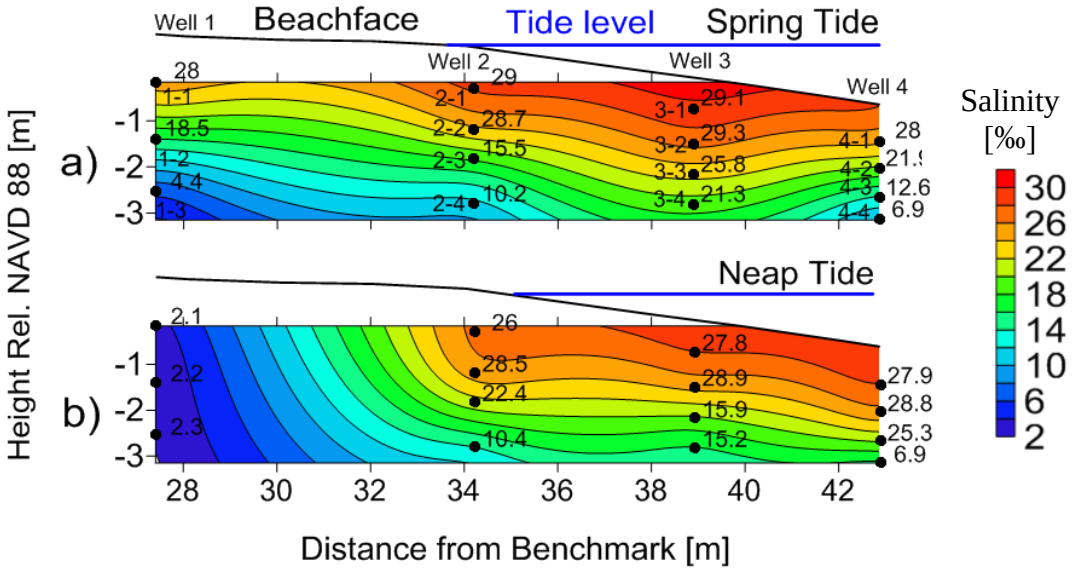

Figure 16. Aquifer response to tidal amplitude. Horizontal blue line marks the tide elevation. a) Salinity distribution during September 2010 spring tide (09/11/2010) and; b) Salinity distribution during October 2010 neap tide (10/1/2010).

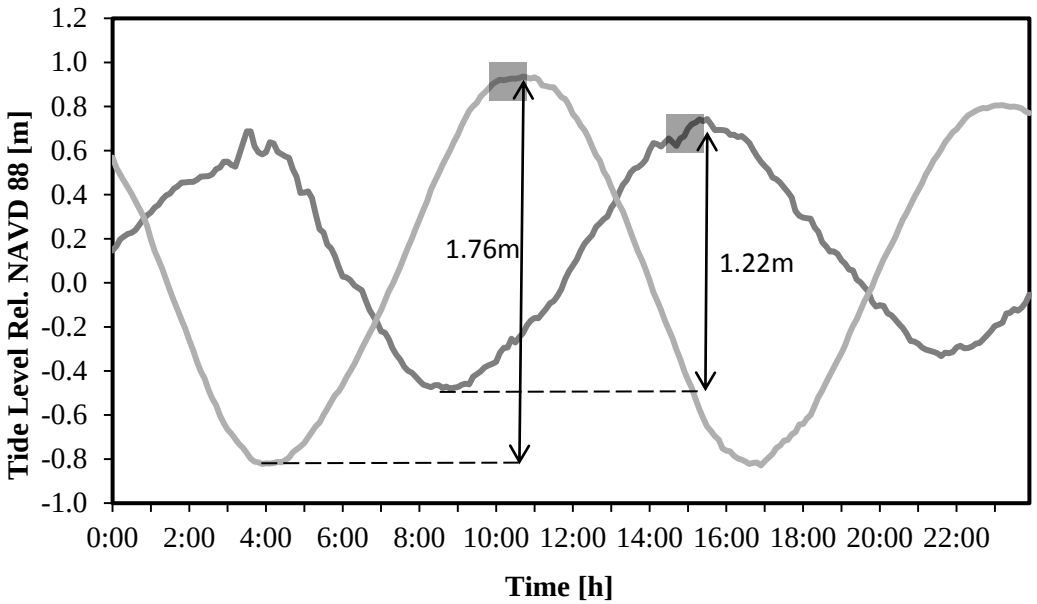

Figure 17. Verified water levels for September 2010 spring tide and October 2010 neap tide. Gray boxes indicate time of sampling. Sea surface elevation was approximately equal during both sample periods to eliminate the effects of short term tidal forcing.

4.1.3 Seasonal Influences

Porewater salinities from September 2010 to May 2011 showed a similar pattern as those observed during the tidal cycle and spring-neap sampling events, however salinity at this time scale appeared to be controlled primarily by inland water table elevation rather than tidal forcing. The response of the beach mixing zone to seasonal fluctuations in inland water table head is evident in figure 18.with the water level elevation 18 km northwest of the study area plotted in Figure 19. Figure 18 shows salt concentrations from 0 to -2.5 m relative to NAVD 88 and 29.5-46 m relative to the benchmark were highest during September after which they decreased 2-4‰ leading up to December. The discharging brackish (8-12ppt) mass from 46-54

m (Figure 18a) underwent a more rapid freshening from 8-10‰ to 4-8‰ from September to December (Figure 18b). Salt concentrations -1.0 to -2.5 m relative to NAVD 88 dropped significantly from December to March while salinity -2.5 m to 4 m from the benchmark increased up to 12‰ over the same period. This response coincides with the inland water table elevation shown in Figure 19. The rise in water table head caused the hydraulic gradient driving freshwater towards the coastline to increase. This resulted in greater freshwater through-flow, dilution, and freshening of the brackish mixing zone. Salinity from 0-3.5 m increased between 34 and 46 m from the benchmark from March to April while the discharging mass 46-51 m from the benchmark freshened to 1-3‰. Subsurface salinity and water table elevation from March to April and May indicate that the circulation cell became more saline as the water table dropped. A shallow and relatively fresh circulation cell can therefore be expected in late winter to spring when inland water tables are high and a deepening of the cell and a salinization of the discharging plume can be expected during summer when inland water tables are low.

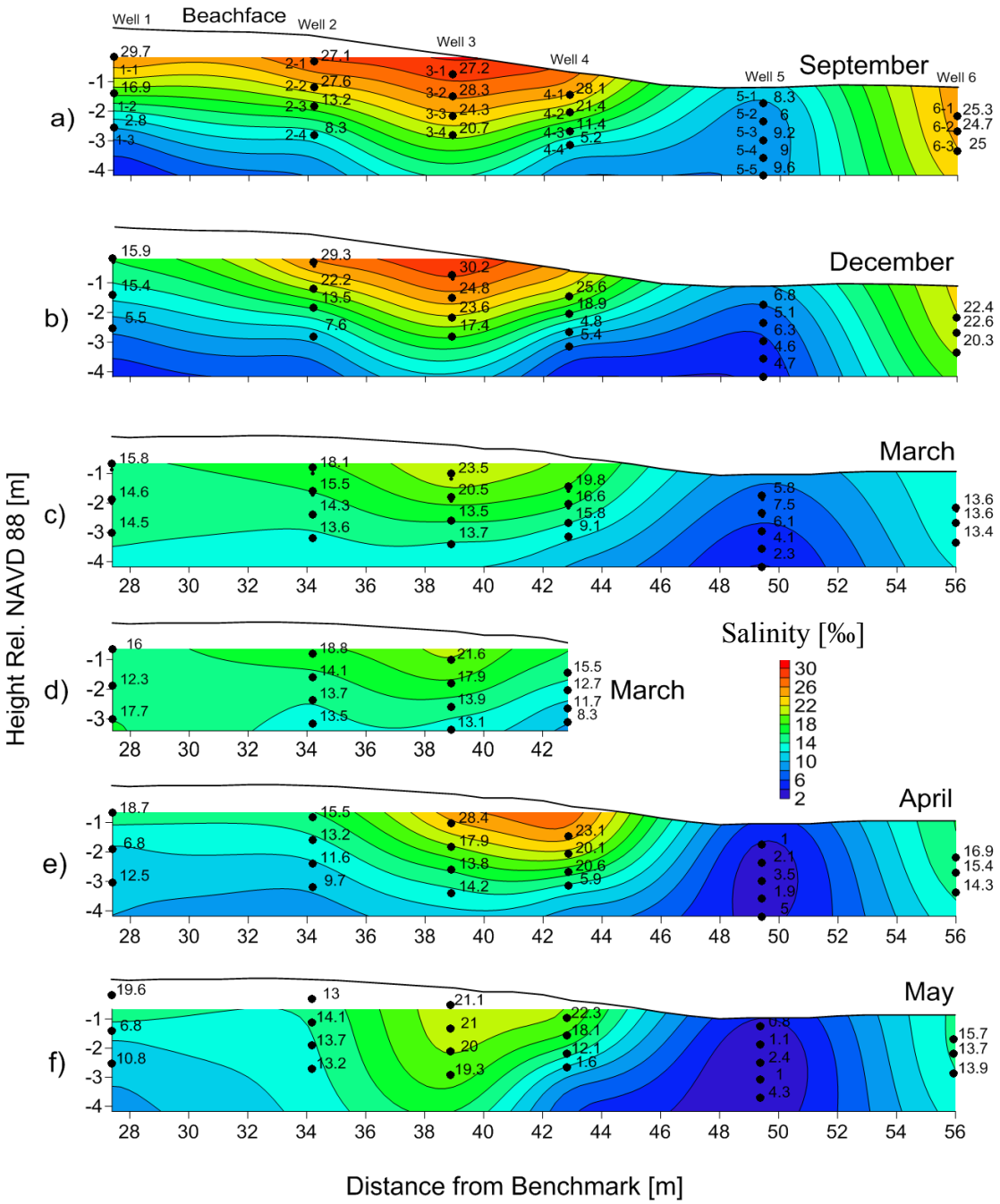

Figure 18. Salinity distribution during low tide from September 2010 to May 2011.Tide level is seaward of cross section so it is not shown. Porewater was sampled during low tide for all cross sections to eliminate the effects of short term tidal forcing.

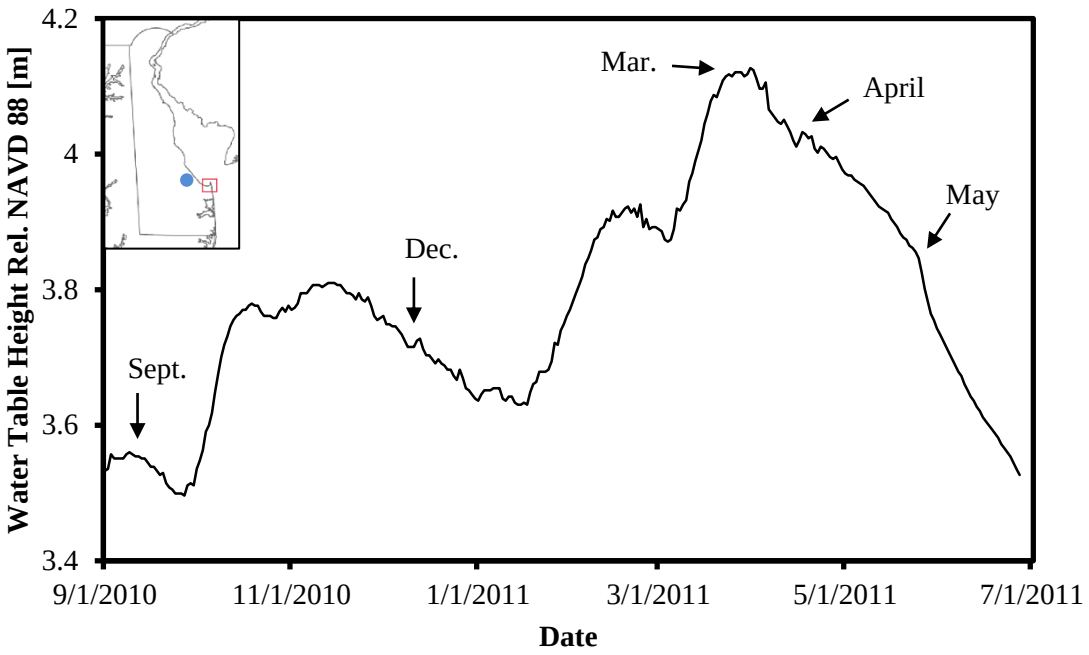

Figure 19. Inland water table elevation with groundwater well marked by blue circle.

4.2 Moisture Content and Water Table Response

The above field measurements indicate that the depth and areal extent of the circulation cell is a function of the tidal stage, tidal amplitude, and inland water level elevation. While this type of characterization is successful at predicting the location and shape of the mixing zone, it does not provide a means of calculating infiltration across the beachface. To accomplish this, moisture sensors were installed to measure the moisture response in the unsaturated zone to wave swash. The moisture content of unsaturated beach sands subjected to wave swash first increases as the bed is inundated by seawater and then decays, first rapidly and then at a slower rate once the sand surface becomes exposed during wave run-down. The difference in moisture content can be equated to the volume, or flux, of seawater that infiltrated into the

beach. The assumptions associated with these calculations are discussed in Section 5.3.

The location and approximate penetration depth of infiltrating seawater can be inferred from an example time series of moisture sensor and pressure sensor data from Station 1 during high tide at the Herring Point site (Figure 20). Snapshots of moisture content and water table position during this experiment are illustrated in Figure 21. When the first swash event (t=6min) inundated the beachface above the sensors, there was a rapid increase in moisture content of VW3 that was followed by a gentler decay. VW2 showed a similar frequency to VW3, but with a dampened response in amplitude. A 40 s phase lag between VW2 and VW3 was evident as the sand surface underwent wetting and dewetting caused by wave run-up and run-down (Figure 20). This offset is evident at t=6min, t=15min, t=17min, and t=20.5min when moisture content surrounding VW3 peaked approximately 40 seconds before VW2. Sediment surrounding VW1 at t=6min was too deep to experience moisture fluctuations (Figure 21a). Instead, pore space in this region slowly filled with water that originated from porewater draining from the overlying sediments. This caused the moisture content near VW1 to rise from t=6min and t=15min until the swash events at t=15min and t=17min resulted in an influx of seawater that caused the sand surrounding VW1 to become saturated (Figure 21b). The moisture responses shown in Figure 20 reveal that the largest moisture content fluctuations took place when only the largest magnitude swash events are able to reach the elevation of the beachface above the sensors. In this case, the period of surficial flooding of the beachface was long enough to allow the

seawater to drain from the variability saturated zone, thereby increasing interstitial pore space until the next swash event.

Volumetric water content fluctuations and water table dynamics show a complex response to wave overtopping (Figure 20). Between t=6min and t=15min, the pressure response and absence of moisture content fluctuations suggest that three swash events (Figure 20) occurred with magnitudes that were insufficient to reach the elevation of the beachface above the sensors but had run-up limits that were high enough to induce a pressure response from the inland propagation of a water table wave. In addition to the lateral inflow of seawater beneath the moisture sensors due to the rising tide, the infiltration caused by these swash events explains the absence of moisture content fluctuations despite a rise of the phreatic surface.

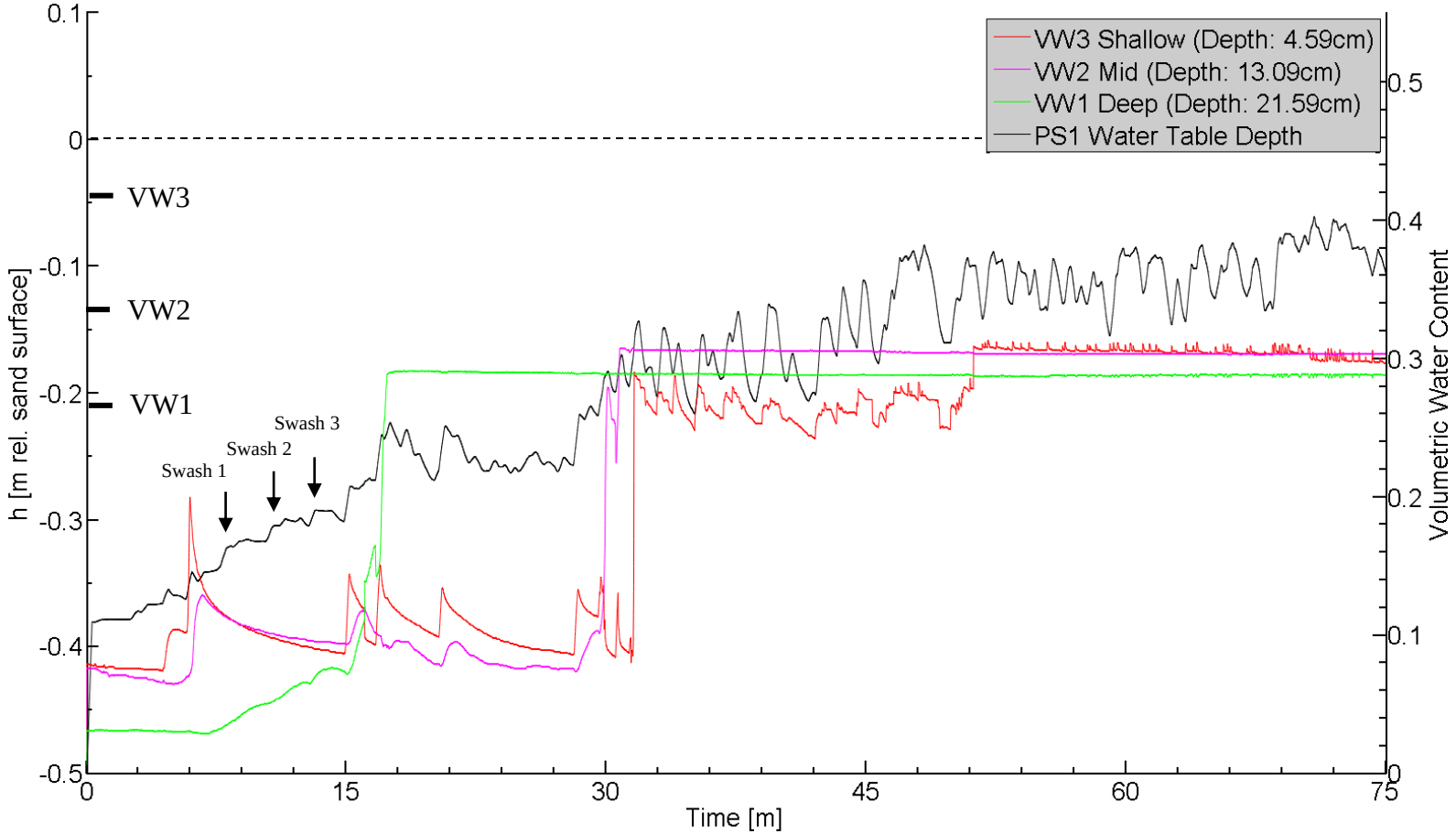

Figure 20. Time series for Station 1 at Herring Point during high tide.

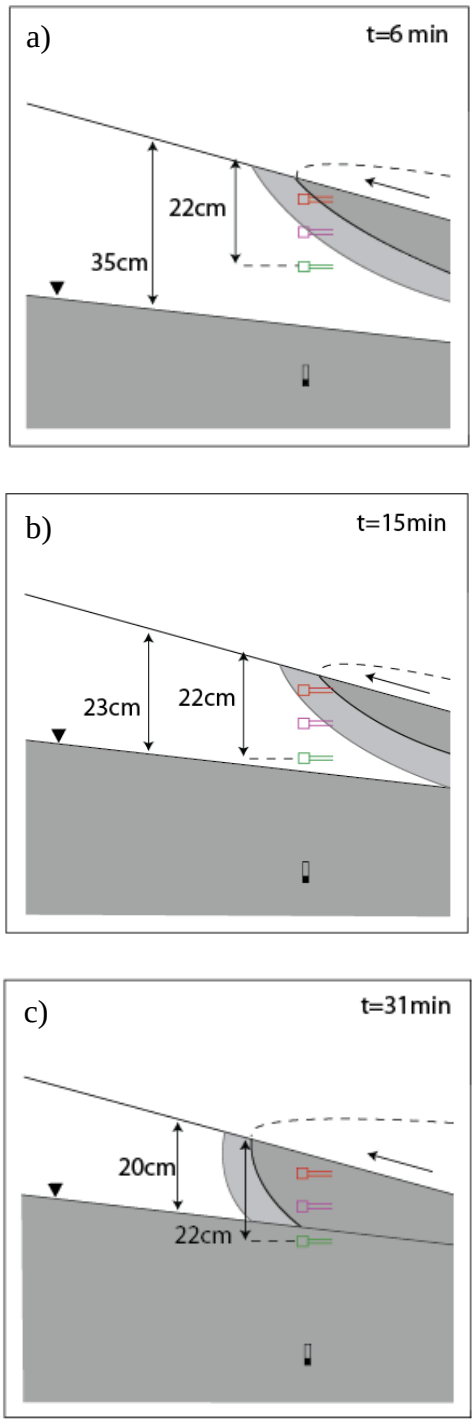

Figure 21. Location and penetration depth of infiltrating water mass due to wave swash at Herring Point during high tide. Sensor color coincides with Figure 20.

Analysis of these data also allows tracking of the capillary fringe thickness during the experiment. From the data in Figure 20 and in the conceptual diagram in Figure 21b, the swash events at t=15min t=17min caused VW1 to saturate at t=17min, suggesting that this is when the top of the capillary fringe came into contact with the sensor. Given that the depth of VW1 was 22 cm and the depth to the water table at this time was approximately 23 cm, it is estimated that the thickness of the fringe was 1 cm. VW2 became saturated t=31min when the depth to the water table was 17.5 cm below the sand surface, suggesting a capillary fringe thickness of 4.5 cm. The top of the capillary fringe reached VW3 at t=51min while the water table was 10 cm below the surface, yielding a thickness of 5.4 cm.

A theoretical steady state thickness of the capillary fringe can be calculated for the average grain size *D* (518μm) of the shallow (0-0.5 m) sediments of Cape Shores following the mathematical model from Equation 5 given by Turner and Nielsen (1997). Using estimated field parameters in Table 2, the theoretical steady state thickness of the capillary fringe ranges from 14.2-14.8cm and is several times greater than the field estimates. The Turner and Nielsen (1997) mathematical model can only be used under steady state scenarios; it was not developed for estimating the thickness of the capillary fringe under transient conditions as was the case during these experiments. The difference between the model and field estimates implies that during transient conditions, the thickness of the capillary fringe may be less than its thickness during steady state.

Table 2. Parameter estimation for capillary fringe thickness.

Parameter	Minimum Value	Maximum Value	Units
$\boldsymbol{\rho}$	1016.9	1022.3	kg/m^3
$\boldsymbol{\alpha}^*$	0.7329	0.7596	dyn/m

*Fluid viscosity calculated from Guohua, et al., 1994

4.3 Swash Induced Infiltration

Swash driven influx must be quantified at both study areas before the intertidal hydrologic conditions and the physical forcing mechanisms that act on the beach aquifer are well characterized. Comparison of infiltration rates across the intertidal zone and between the two field sites will help determine what hydrologic factors influence swash influx.

Swash-induced infiltration rates at MLLW and MHHW at the Cape Shores and Herring Point study areas are shown in Figure 22. The experiments demonstrate that infiltration at these sites is likely a function of the cross shore position in the intertidal zone and may be dependent on maximum wave run-up. Infiltration was highest near MHHW and lowest near MLLW at both study sites so the rates can be used as the upper and lower bounds for infiltration, respectively. Swash induced seawater influx at Cape Shores was 7.05×10^{-6}m/s at high tide and 2.60×10^{-6}m/s at low tide. At Herring Point, swash driven infiltration was 1.62×10^{-5}m/s at high tide and 1.03×10^{-5}m/s at low

tide. In order to compare these estimates to the analytical solution given by Li et al., 1999, the infiltration rates were integrated over half of a tidal cycle.

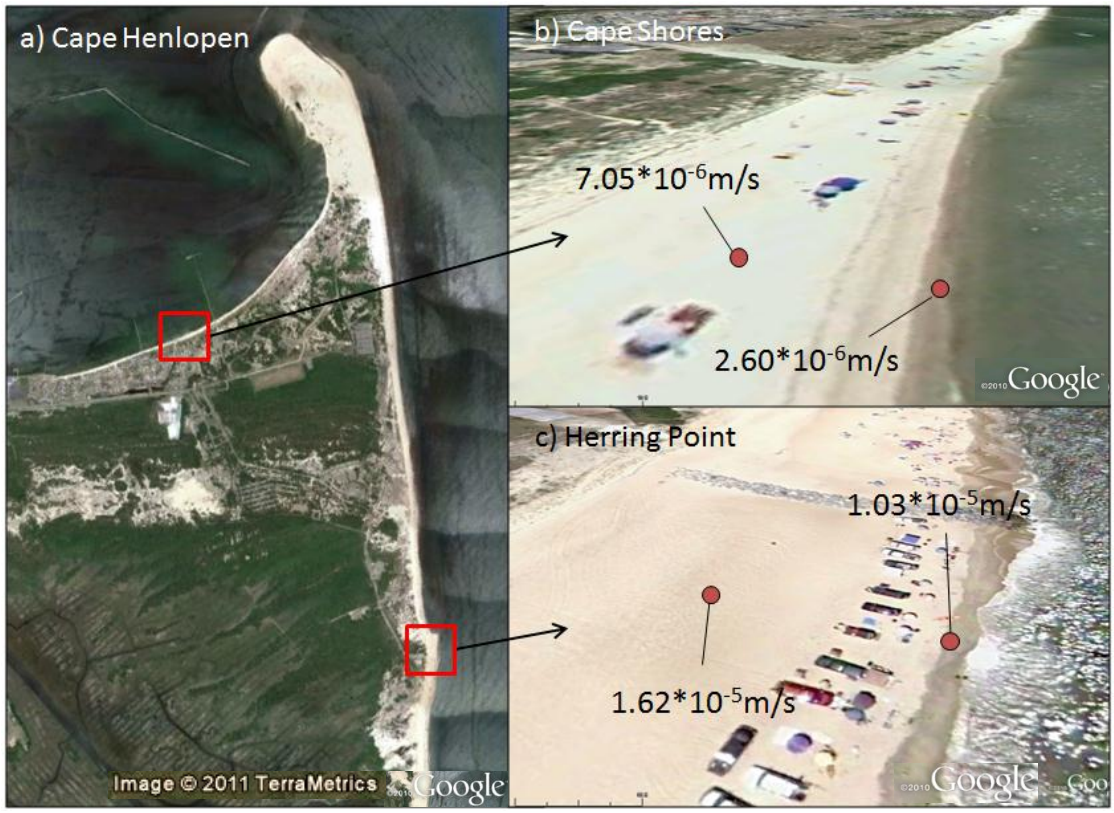

Figure 22. a) Cape Henlopen study areas; b) infiltration rates at the low and high water marks at Cape Shores and; c) Herring Point.

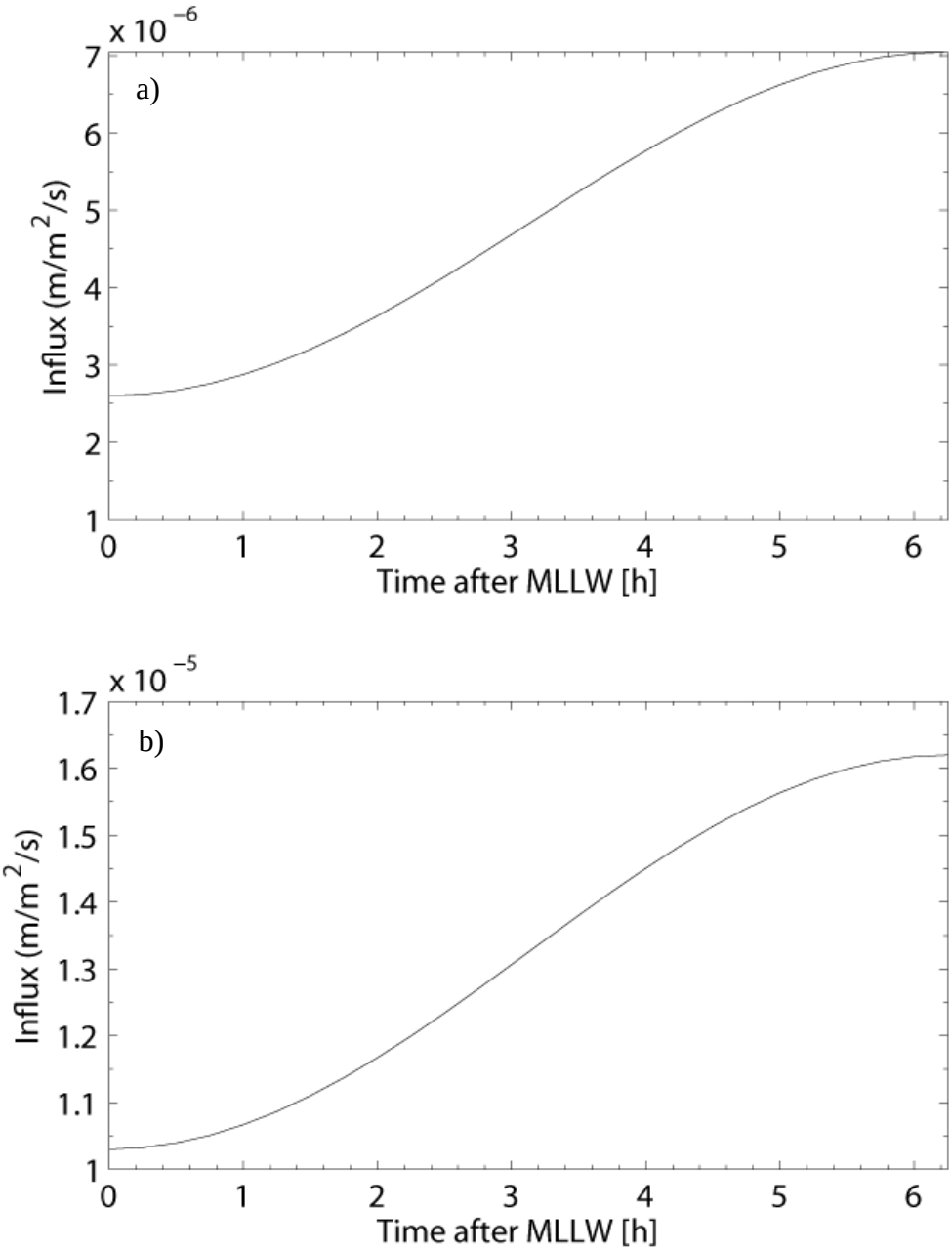

Figure 23. Swash induced seawater influx as a function of time at a) Cape Shores and b) Herring Point.

A cosine function can be used to describe the superposition of the tidal harmonics as measured by the Lewes gauge station for the height of the tide beginning at high water and decreasing to low water. A series of phase, period, and amplitude shifts applied to the cosine curve were used to describe the height of the tide during a rising tide as a function of time over a period of half a tidal cycle. The reasoning behind this premise is that it is assumed that the development of a seepage face during ebb tide prevents infiltration during the second half of the tidal cycle. Equation 18 describes the height *h* of the tide as a function of time *t*:

$$h_{tide} = \left(\frac{Diurnal\ Range}{2}\right)\left(1 + \cos\left(\left(\frac{2\pi}{12.5}\right)t + \pi\right)\right) \tag{18}$$

$$R_t = \left(\frac{R_{max} - R_{min}}{Diurnal\ Range}\right)\left(\frac{Diurnal\ Range}{2}\right)\left(1 + \cos\left(\left(\frac{2\pi}{12.5}\right)t + \pi\right)\right) \tag{19}$$

It is assumed that the relationship between tidal height and infiltration rate is linear due to the fact that only the maximum and minimum rates were measured. Future work is needed in order to improve these estimates. The linear coefficient was then incorporated into Equation 18 to yield Equation 19, which expresses infiltration rate *R* as a function of time *t* with the maximum (R_{max}) and minimum (R_{min}) infiltration rates as measured in the field and the diurnal tidal range as measured by the Lewes tidal gauge station. Infiltration rates estimated by Equation 19 are plotted in Figure 23 for Cape Shores and Herring Point using a diurnal tidal range of 1.42m. Integrating Equation 19 yields an influx of 0.11m^3 per tidal cycle per meter length of shoreline at Cape Shores and 2.03m^3 per tidal cycle per meter length of shoreline at Herring Point.

4.4 Swash-Induced Hydraulic Gradients

An example time series of hydraulic gradients between Station 1 and 4 at the low energy Cape Shores site during high tide is plotted in Figure 24 and conceptually illustrated in Figure 25. A positive hydraulic gradient is indicative of seaward flow and a negative gradient indicates landward flow. Hydraulic gradients across the swash zone reversed direction as the tide lifted the swash zone to the upper regions of the beachface. The initial hydraulic gradient between each consecutive sensor was greater than zero, indicating seaward directed flow across the array. Hydraulic gradients between each sensor began to decline, initially gently and then more rapidly as larger magnitude swash events began reaching the elevation of the beachface above the sensors (not shown in Figure 24, but illustrated in Figure 25).

At t=60 minutes, the hydraulic gradient and flow direction between Station 1 and Station 2 reversed from seaward to landward at which point there was a small magnitude seaward directed gradient between Station 2 and Station 3 (0.004) and stronger seaward flow (0.018) between Station 3 and Station 4 (Figure 24a-c). The magnitude of landward flow between Station 1 and Station 2 increased until a maximum landward hydraulic gradient of -0.007 was recorded at t=75, indicating landward flow (Figure 24b). The negative gradient between Station 1 and Station 2 returned to zero at t=90 while the gradient between Station 2 and Station 3 (-0.003) reversed to indicate the onset of landward flow between these two sensors. A positive gradient (seaward flow) between Station 1 and Station 2 (0.003) was reestablished at t=105 while the gradient between Station 2 and Station 3 was zero. Water levels

between Station 3 and Station 4 suggested landward flow during this same time period (Figure 24c).

Swash zone hydraulic gradients at Herring Point during high tide are shown in Figure 26 and conceptually illustrated in Figure 27. In addition to experiencing a substantially longer period of landward flow, the magnitude of hydraulic gradients at Herring Point had a larger range than Cape Shores. Hydraulic heads measured by the buried pressure sensors indicated negative gradients between each station at t=30. The zone with the largest magnitude landward hydraulic gradient migrated landward from t=30 to t=60 and was observed to be between Station 3 and Station 4 at t=60. All gradients pointed landward at t=90; however their magnitude decreased as infiltrating seawater sequentially filled the pore spaces between Stations 1 and 4. The magnitude of landward flow between Station 3 and 4 decreased from t=90 m to t=120 m while the gradient between Station 2 and 3 reversed from landward flow to one with a net flow seaward. The gradient between Station 1 and 2 at t=120 m was seaward, indicating a groundwater divide below Station 3.

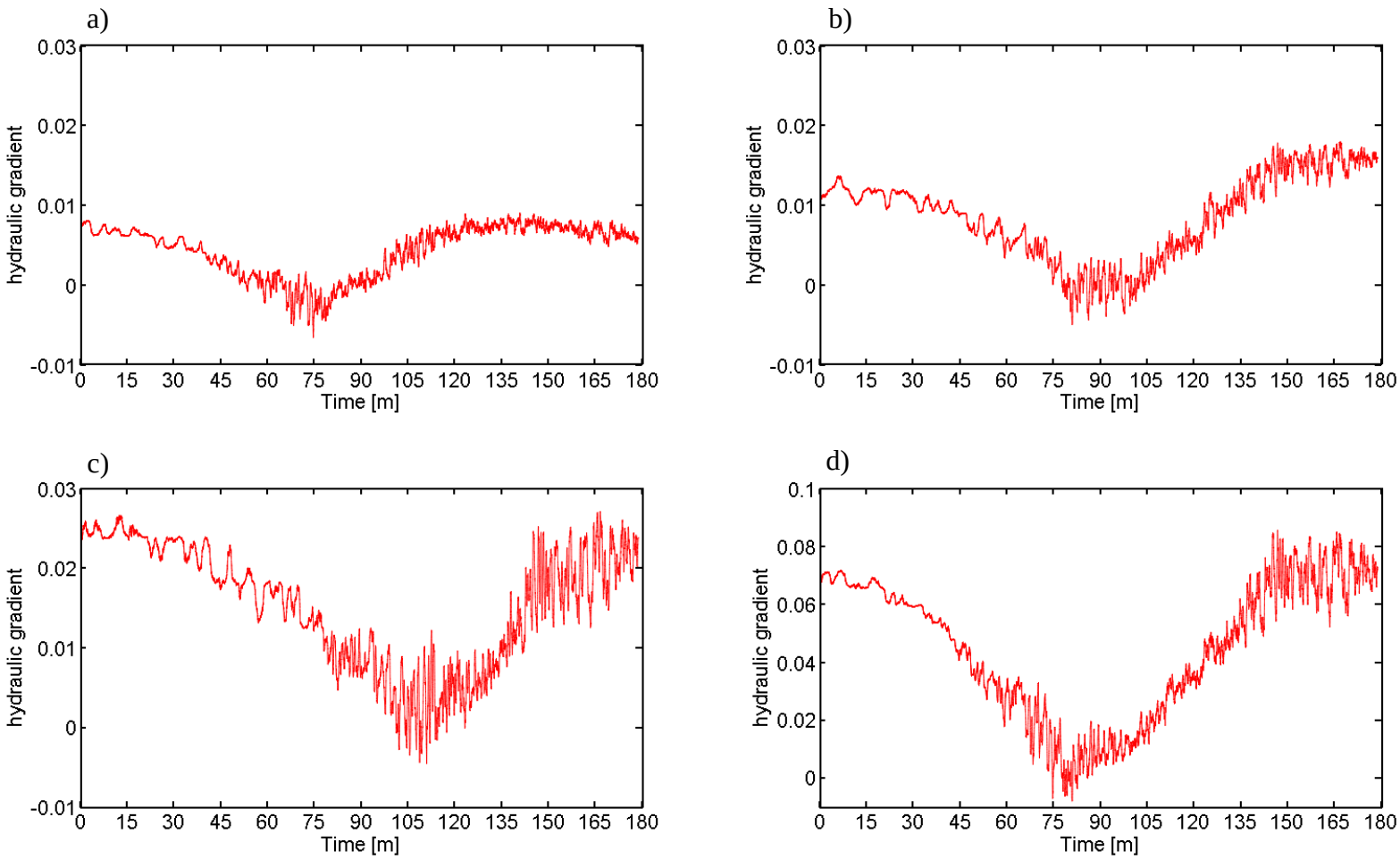

Figure 24. Swash zone hydraulic gradients at Cape Shores near high tide between a) Station 1 and Station 2; b) Station 2 and Station 3; c) Station 3 and Station 4 and; d) Station 4 and Station 1. Positive values indicate seaward flow.

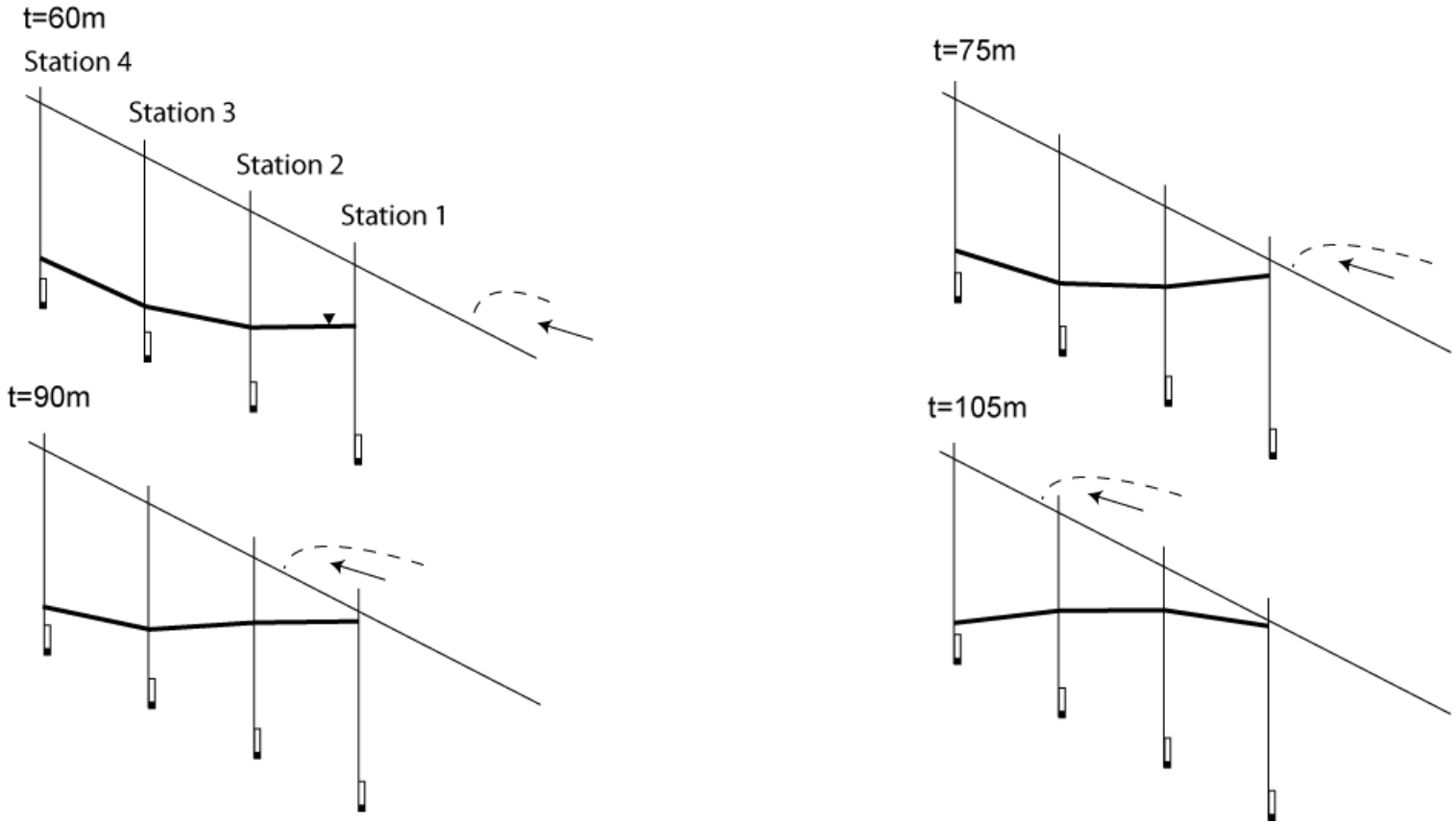

Figure 25. Cape Shores schematic of hydraulic gradients at high tide from t=60 to t=105 minutes. Not to scale.

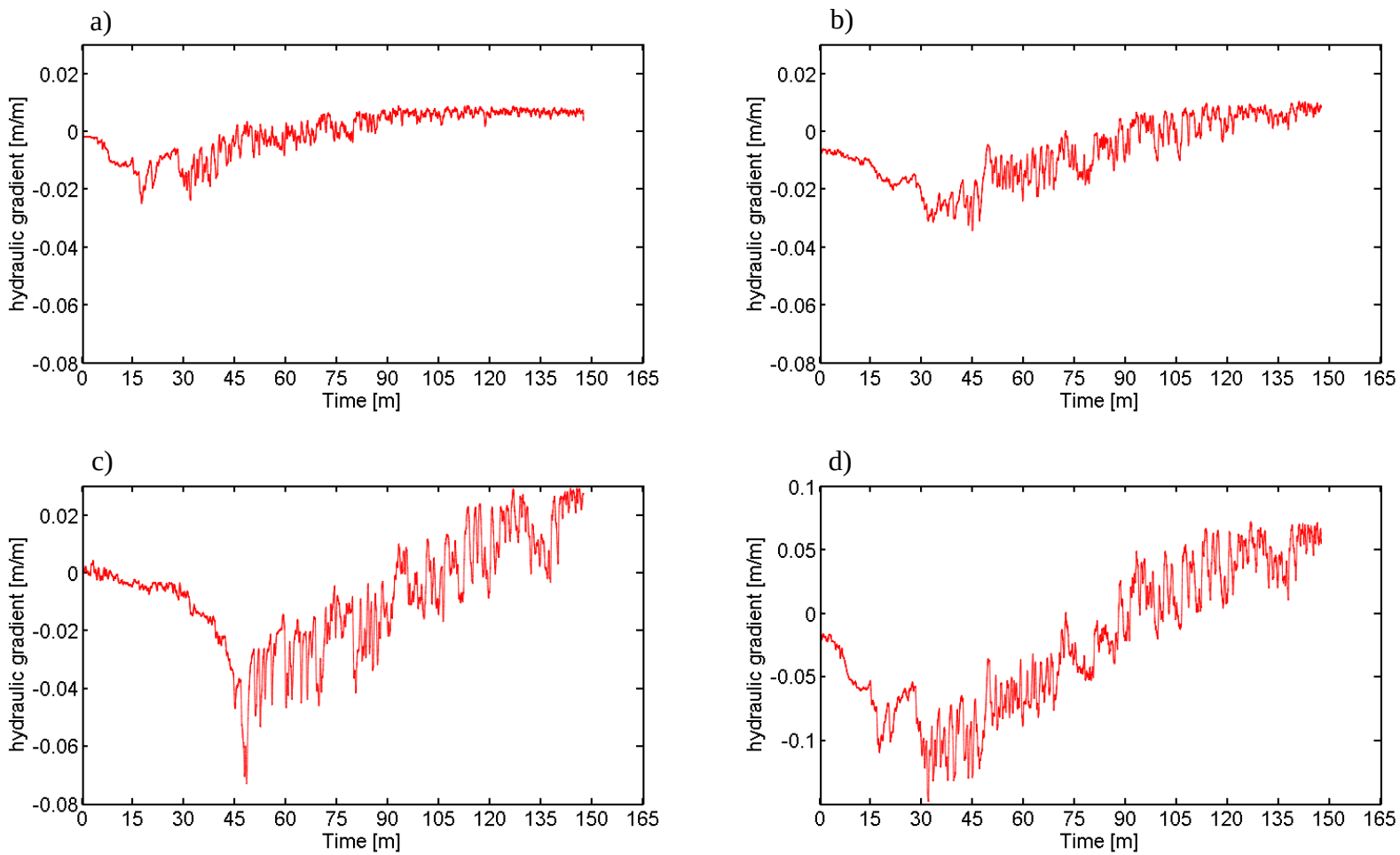

Figure 26. Swash zone hydraulic gradients at Herring Point near high tide between a) Station 1 and Station 2; b) Station 2 and Station 3; c) Station 3 and Station 4 and; d) Station 4 and Station 1. Positive values indicate seaward flow.

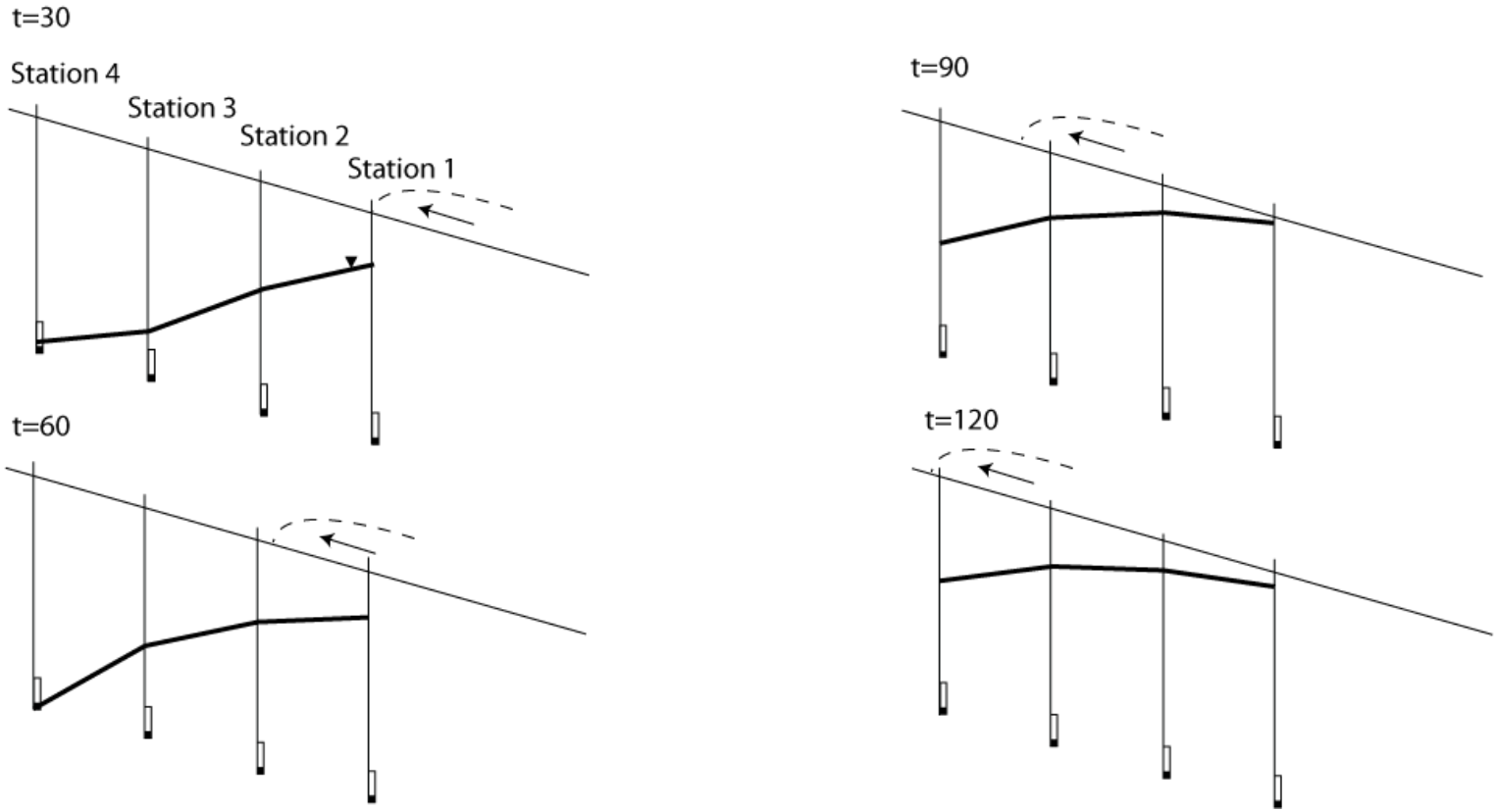

Figure 27. Herring Point schematic of hydraulic gradients at high tide from t=30 to t=120 minutes. Not to scale.

Chapter 5

DISCUSSION

The results of this investigation reveal that microtidal sandy beaches can host subsurface brackish mixing zones that respond to tidal and seasonal hydraulic forcing at time scales ranging from hours to months. Furthermore, swash-induced influx of seawater has been shown to control the saturated and unsaturated behavior of sediment beneath the swash zone. While prior work has been directed towards investigating coastal groundwater mixing and its implications on the geochemical conditions in coastal aquifers, only few authors (e.g. Robinson et al., 2006; Robinson et al., 2007; Urish and McKenna, 2004) have investigated the hydraulic mechanisms that affect the spatial and temporal geometry of the transition zone.

5.1 Tidal Effects on Intertidal Subsurface Mixing

This study confirms previously published results on the effects of tides on beach groundwater dynamics by verifying the manifestation of a brackish-saline mixing zone with circulating flow driven by a super-elevation of the water table. These findings agree well with the numerical model developed by Robinson et al. (2007a) of a beach aquifer subjected to tidal undulation. Field observations from Cape Henlopen, DE presented in this thesis indicate that the overlying brackish mixing zone

can penetrate up to 4 m below the beach surface (Figure 13), while salt concentrations under steady-state conditions in Robinson et al. (2007a) suggest tidally oscillating flows can induce downward directed flow of seawater to depths of up to 5 m. Parametric analysis of tidal amplitude in Robinson et al. (2007a) corresponds with our observations that the depth and horizontal extent of the mixing zone increases with tidal amplitude. Their study indicates through particle tracking that as the mixing zone extends farther inland under larger tidal amplitude conditions, the transit times for circulating seawater increase. Although the study presented here does not attempt to quantify travel times, it can be inferred from Figure 16 that flow paths from the upper beachface to the discharge zone during spring tide would result in longer transit times than during neap tide. A similar field investigation by Robinson et al. (2007b) revealed a well-defined intertidal circulation cell with salinities that varied significantly from spring to neap tide. Compared to the present study, the maximum penetration depth of the cell (0-1.3 m) occurred during spring tide even shallower depths (0-0.5m) during neap tide. This is three to five times shallower than the penetration depth observed at the Cape Shores site. Although there are a number of hydrogeologic factors that may be contributing to this discrepancy, including heterogeneity, mean grain size, and beach slope, variation in the shape, size, and temporal response of the cell to tidal forcing provide an indication that the mixing zone can be sensitive to variety of hydraulic conditions. These include tidal amplitude, wave action, and freshwater forcing.

Ataie-Ashtiani et al., (1998) used a variable density groundwater model to simulate the effects of tidal fluctuations on the thickness and position of the saltwater-freshwater interface and found that tidal fluctuations cause seawater infiltration across the beachface near high tide to form a thicker interface in the shallow regions of the aquifer than would otherwise occur in the absence of tidal activity. The subsurface salinity distribution at the Cape Shores site suggests that discharging freshwater near low tide can divide the upper portion of the interface to form a brackish beach circulation cell that is separate from the landward edge of the Ghyben-Herzberg interface (Figure 17c). In a situation where there is less offshore freshwater discharge, it might be expected that the circulation cell would remain part of the deeper traditional interface to form a thicker zone of dispersion near the surface as described by Ataie-Ashtiani et al., (1998).

5.2 Wave Swash and Tidal Effects on Infiltration Across the Beachface

In addition to tidal induced SGD, wave forcing will also act on the beach aquifer to induce circulated flow that will contribute to total SGD. Tidal and swash induced SGD can be estimated using Equation 4 from Li et al., (1999) and a range of parameters applicable to a natural coast. Tables 3 and 4 provide the estimated parameter values for calculating groundwater circulation due to tidal and wave activity at the Cape Shores and Herring Point study areas, respectively. The minimum value for each parameter represents the lowest estimate and the maximum value represents the highest estimate that would be expected at both study sites. The

observed/estimated value was measured in the field or in the lab. Maximum and minimum parameters that were not measured were estimated based on values characteristic of sandy beaches along the East Coast. Tables 3 and 4 show integrated infiltration rates over a rising tide, which as a result of a seepage face during ebb tide, is assumed to be the total infiltration rate over a full tidal cycle. Estimated wave driven SGD for the Cape Shores study area is $0.36m^3$ per tidal cycle per meter length of shoreline, which agrees reasonably well with $0.11m^3$ as measured in the field given the parameter uncertainties and assumptions of the analytical solution and field measurements. Calculated infiltration for Herring Point is 2.07 m^3 per tidal cycle per meter length of shoreline compared to only $0.3m^3$ as measured in the field.

Field measurements and model estimates demonstrate that wave setup may contribute to significant rates of SGD; however the calculated rates have high uncertainty. The range of parameters and discharge estimates vary by several orders of magnitude which emphasizes the importance of incorporating sufficient field data in order to closely approximate true discharge rates. Better estimates of hydraulic conductivity, aquifer thickness, and average breaker height are needed to reduce these uncertainties. Parametric analysis of the equations given by Li et al. (1999) indicate that the values are most sensitive to the breaker height; maintaining the Herring Point parameters in Table 3, but setting this parameter equal to the observed breaker height at Cape Shores results in an estimate that is $0.10m^3$ (71.3% of Cape Shores calculated discharge) less than the observed value at Cape Shores, which is an 87.8% decrease.

The relative percent contribution of seawater to the circulation cell due to waves and tides at Cape Shores can be estimated using the measured and calculated infiltration and discharge rates. The average cross sectional area of the cell is estimated to be 52.5 m^2. Using a porosity of 0.3 (observed on 03/25/2011), a swash driven infiltration rate of 0.11 m per tidal cycle (measured in the field), and 1.94 m of discharge per tidal cycle due to tides (calculated from Li et al. 1999), it is estimated that wave swash and tidal forcing contribute 5.4% and 94.6% of bay water to the circulation cell, respectively. Using the Li et al. (1999) approximations for maximum and minimum discharge rates due to tides, and 0.11 m for wave swash as measured in the field, this falls in the range of 0.6% to 30.9% contributed by waves and 40.6% to 99.4% contributed to the cell by tides.

A similar calculation can be used to estimate percent contribution of discharge from waves and tides at Herring Point. Using the observed/estimated discharge rates calculated from the Li et al. (1999) solution, approximately 54.3% of discharge is due to waves, while only 45.7% is the result of tides. Using the calculated maximum and minimum discharge rates, this is in the range of 9.5% to 89.1% contributed by waves and 10.9% to 90.5% caused by tides. Compared to the percent contribution to discharge from waves at Cape Shores, the larger breaker height associated with Herring Point is responsible for a significantly larger percent contribution while maintaining a similar tidal range: more than half of the observed/estimated discharge at Herring Point is due to waves while just over 5% can be attributed to waves at Cape Shores.

Table 3. Parameters and calculated values for tidal and wave circulation at Cape Shores.

Parameter	Minimum Value*	Maximum Value*	Observed/Estimated Value*	Units
η_e	0.2	0.5	0.3†	-
A	0.61	0.89	0.75‡	m
T_t	44700	44700	44700†	s
s_b	0.15	0.01	0.123†	-
H	4	30	17	m
K	1×10^{-6}	9×10^{-4}	3.41×10^{-4} §	m/s
H_b	0	0.2	0.09	m
T_w	0.5	5	2.5ȣ	s
D_t	0.25	19.7	1.94	m^3/ tidal cycle
D_w	0	1.29	0.36	m^3/ tidal cycle

* All values estimated unless otherwise noted
† Observed on 03/25/2011
‡ Measured by Lewes, DE 8557380 tidal gauge station
§ Calculated from permeameter tests
ȣ Observed on 10/08/2009

Table 4. Parameters and calculated values for tidal and wave circulation at Herring Point.

Parameter	Minimum Value*	Maximum Value*	Observed/Estimated Value*	Units
η_e	0.2	0.5	0.3†	-
A	0.61	0.89	0.75‡	m
T_t	44700	44700	44700†	s
s_b	0.15	0.01	0.047†	-
H	4	30	17	m
K	1×10^{-6}	9×10^{-4}	1×10^{-4} §	m/s
H_b	0	1.5	1	m
T_w	2	12	9.5ȣ	s
D_t	0.25	19.7	1.67	m^3/ tidal cycle
D_w	0	9.66	2.07	m^3/ tidal cycle

* All values estimated unless otherwise noted
† Observed on 01/29/2011
‡ Measured by Lewes, DE 8557380 tidal gauge station
ȣ Observed on 05/07/2010

It is intriguing to speculate why the inflow of seawater caused by wave swash was not perpendicular to the sand surface (Figure 21). One possible explanation is anisotropy which could result in a greater intrinsic permeability parallel to the beachface. This would induce a horizontal flow component and create a flow pattern that is not normal to gravity (Figure 21). The movement of the groundwater mass may also have been due to the distribution of hydraulic head caused by the wave swash and the slope of the beachface.

Shallow infiltrating seawater near maximum wave run-up results in higher head than infiltrate near the bottom of the swash zone. The difference in head can be attributed to the slope of the beachface caused by the change in elevation from the top to bottom of the swash zone. The resulting hydraulic gradient is seaward with a magnitude that is partly dependent on the slope of the sand surface.

5.3 Assumptions

There are two operational parameters that may be contributing to calculated moisture flux across the sediment surface that do not represent true infiltration rates. A major assumption when integrating and summing volumetric moisture content fluctuations is that the rise and decay of moisture content of sediment surrounding a sensor is solely due to “new” seawater that did not originate from sediment surrounding adjacent sensors. It is assumed that there is no fluid exchange between the cells used to calculate flux. If this were not the case and the decline of moisture

content in shallow sediment was due to the drainage of the porewater to deeper sediments, then the rise in moisture measured by the deeper sensor would contribute to an overestimate of the true influx by an amount equal to the volume of seawater exchange between the adjacent cells. There is a 40 second lag between moisture content peaks of VW2 and VW3 during the first swash event at t=15min (Figure 21). This time lag is also evident in the moisture signals that follow and suggests that porewater exchange may be taking place. The influx estimates may therefore be over estimating true influx rates. Nonetheless, the angled flow path from the beach surface to the sensors may imply that this is not the case and that the infiltrating seawater takes 40 seconds longer to reach the bottom sensor.

The second operational parameter that may be contributing to apparent moisture flux across the sediment surface is mass loading. The water mass of a swash event that inundates the sand surface will apply a downward stress on the sand matrix that is a function of the depth and density of the wave run-up event. The storativity of the aquifer will thus fluctuate with the expansion and contraction of the sediment skeleton and generate a change in volumetric moisture content that is unrelated to fluid flow though the bed. Since this effect is likely negligible relative to total flux, it is assumed that the moisture fluctuations are due exclusively to the influx and subsequent drainage of seawater and that not to changes in storativity caused by changes in porosity.

It is also assumed that infiltration ceases during ebb tide. This assumption is supported by field observations during ebb tide at the Cape Shores and Herring Point

sites which showed that the rate of tidal fall exceeded the rate of water table fall, forming an exit point. The sediment seaward of this point remained saturated this preventing fluctuations in moisture content.

5.4 Implications

This study reveals that tidal oscillating flows and swash induced infiltration are important forcing mechanisms contributing to beach groundwater dynamics. The work provides new insight into beach surface water-groundwater interaction and reveals that sandy beaches can host brackish mixing zones. Furthermore, a new method for quantifying swash-induced seawater infiltration has been presented and tested that may have important uses in quantifying a primary chemical transport pathway that leads to the zone of reactivity.

The expansion and contraction of the mixing zone may have profound effects on subsurface biogeochemical activity. Through-flowing fresh water derived from upland sources is often rich in nitrogen in the form of NO_3^-, anoxic, but devoid of reactive organic matter. Organic carbon that is transported in seawater along intertidal groundwater flow paths from the beach surface to the mixing zone may provide the missing organics that denitrifying bacteria require for metabolic processes. Mixing of these water masses may therefore mediate the discharge of oxidized forms of bioavailable nitrogen. Thus the amount of bioavailable nitrogen in estuaries is preferentially removed through the biological reduction of NO_3^- and NO_2^- to N_2O and N_2 gas.

The oscillating geometry of the mixing zone may also have important implications on chemical transformations associated with microbial habitats. If the microbes responsible for beach reactivity are highly sensitive to their surrounding salt concentrations, the hydrologic mechanisms that control the mixing of groundwater masses of varying salinities will likely play a major role in determining what types of organisms inhabit the mixing zone (Santoro, 2009).

Chapter 6

CONCLUSION

This study presents and discusses the response of two sandy beach aquifers to tidal and seasonal hydrologic forcing and quantitatively estimates swash induced infiltration. It is evident that these forcing mechanisms, which operate on time scales ranging from seconds to months, influence subsurface mixing of fresh and saline water masses and that the dynamic nature of these processes can act on beach aquifers to influence the geometry and temporal variability of the circulation cell. Field experiments using high-frequency measurement techniques reveal that wave swash can drive an influx of seawater through the unsaturated zone with rates that vary across the beachface. Infiltration was highest near the top of the tidal cycle and lowest near the bottom while a wider swash zone was shown to have more infiltration than a narrow one. The following is a summary of the major findings that support these conclusions.

1. Sandy beaches subjected to tidal forcing can develop a brackish circulation cell with fluctuating salinity that experiences a 2-3 hour lag relative to the tidal stage. Measurements of subsurface salinity distribution indicate that a larger tidal amplitude

introduces a greater volume of seawater into the upper beach that laterally expands the circulation cell perpendicular to the shoreline and increases the size of the mixing zone.

2. Seasonal variation in upland water table elevation can control beach aquifer salinity. Changes in water table head that result in a stronger hydraulic gradient can be expected to reduce the salinity of the circulation cell due to freshwater dilution and/or greater freshwater through-flow.

3. Swash induced seawater infiltration is a function of the cross shore position in the intertidal zone and the width of the swash zone; seawater influx near MHHW was greater than infiltration near MLLW and integrated infiltration rates were higher at the study area with the widest swash zone.

This thesis presents new methodologies and proof of concept in characterizing and quantifying tidal and wave induced beach groundwater flow. The results of this investigation will help beach managers to assess the need for beach preservation and will benefit coastal engineers in understanding the physical processes that may affect beach morphology and sediment transport. Dynamic mixing between subsurface water masses as shown here may serve as an important pathway for new chemicals as this region may be associated with shorter transit times and faster flow rates than the traditional saltwater-freshwater interface. More specifically, this work will aid in

understanding the geochemical transformations and absorption processes of through-flowing reactive substances that moderate fluxes of chemical contaminants to the coastal zone. The fate of many toxins and their likelihood of damaging fragile coastal ecosystems are determined as they flow through the beach subsurface. Further, because many geochemical cycles are inherently linked to other elemental cycles, a clearer understanding of the underlying hydrodynamics and surface water-groundwater interactions that promote and these linkages will aid in understanding chemical ocean budgets. Therefore recognizing the physical processes that create the conditions necessary for geochemical processes to take place will ultimately help preserve near-shore systems and the recreational and economic benefits associated with sandy beach environments.

REFERENCES

Ataie-Ashtiani, B., R.E. Volker, and D.A. Lockington (2001), Tidal effects on groundwater dynamics in unconfined aquifers, *Hydrological Processes*, 15(4), 655-669.

Austin, M.J., and G. Masselink (2006), Swash–groundwater interaction on a steep gravel beach, *Continental Shelf Research*, 20, 2503-2519.

Baldock, T.E., A.J. Baird, D.P. Horn, and T. Mason (2001), Measurements and modeling of swash-induced pressure gradients in the surface layers of a sand beach, *Journal of Geophysical Research*, 106(C2), 2653-2666.

Black, C.A., 1965, Methods of Soil Analysis: Part I Physical and mineralogical properties,*American Society of Agronomy*, Madison, Wisconsin, USA.

Baird, A.J., and D.P. Horn (1996), Monitoring and modeling groundwater behavior in sandy beaches, *Journal of Coastal Research*, 12, 630-640.

Blewett, J.C., P. Holmes, and D.P. Horn (2001), Field measurements of swash on gravel beaches, *Coastal Dynamics*, 828–837.

Butterworth, B. (1930), On the Theory of Filter Amplifiers, *Experimental Wireless and the Wireless Engineer*, 536-541.

Burnett, W.C., P.K. Aggarwal, A. Aureli, H. Bokuniewicz, J.E. Cable, M.A. Charette, E. Kontar, S. Krupa, K.M. Kulkarni, A. Loveless, W.S. Moore, J.A. Oberdorfer, J. Oliveira, N. Ozyurt, P. Povinec, A.M.G. Privitera, R. Rajar, R.T. Ramessur, J. Scholten, T. Stieglitz, M. Taniguchi, and J.V. Turner (2006), Quantifying submarine groundwater discharge in the coastal zone via multiple methods. *Science of the Total Environment*, 367, 498–543.

Cartwright, N., T.E. Baldock, P. Nielsen, D.S. Jeng, and L. Tao (2006), Swash-aquifer interaction in the vicinity of the water table exit point on a sandy beach,*Journal of Geophysical Research*, 111(C09035), 1-13.

Crist, J.T., J.F., McCarthy, Y. Zevi, P. Baveye, J.A. Throop, and T.S. Steenhuis (2004), Pore-Scale Visualization of Colloid Transport and Retention in Partly Saturated Porous Media, *Vadose Zone Journal*, 3(2), 444-450.

Dean, R.G., and R.A. Dalrymple, *Water wave mechanics for engineers and scientists*, 353 pp., World Sci., Singapore, 1991.

Drabsch, J. (1999), The Capillary Fringe and the Water Table in an Intertidal Estuarine Sand Flat, *Estuarine, Coastal, and Shelf Science*, 48(2), 215-222.

Ehrenhauss, S., and M. Huettel (2004), Advective transport and decomposition of chain-forming planktonic diatoms in permeable sediments, *Journal of Sea Research*, *52*(3), 179-197.

Folk, R.L. (1974), Petrology of Sedimentary Rocks: Austin, Hemphill Publishing Company, 182.

Guohua, C., S. Jingzeng, G. Ling, and Z. Lijun (1994), Study on the surface tension of seawater. *Oceanologia et LimnologiaSinica*, 25(3), 306–311.

Hays, R.L., and W.J. Ullman (2007), Dissolved nutrient fluxes through a sandy estuarine beachface, Cape Henlopen, Delaware, USA: Contributions from fresh groundwater discharge, seawater recycling, and diagenesis, *Estuaries and Coasts*, 30, 710-724.

Heathershaw, A.D., A.P. Carr, M.W.L. Blackley, and C.F. Wooldridge (1981), Tidal variations in the compaction of beach sediments, *Mar. Geol*., 41, 223-238.

Hegge, B.J., and G. Masselink (1991), Groundwater-table responses to wave run-up: an experimental study from Western Australia, *Journal of Coastal Research*, 7(3), 623-634.

Hegge B.J., and G. Masselink (2010), Groundwater-table response to wave run-up: an experimental study from Western Australia, *Journal of Coastal Research*, 7(3), 623-634.

Henderson, R.D., F.D. Day-Lewes, E. Abarca, C.F. Harvy, H.N. Karam, L. Liu, J.W. Lane, Jr. (2010) Marine electrical resistivity imaging of submarine groundwater discharge: sensitivity analysis and application in Waquoit Bay, Massachusetts, USA, *Hydrogeology Journal*, 18, 173-185, DOI 10.1007/s10040-009-0498-z.

Horn, D.P. (2002), Mesoscale beach processes, *Progress in Physical Geography*, 26(2), 271-289.

Horn, D.P. (2006), Measurements and modeling of beach groundwater flow in the swash-zone: a review, *Continental Shelf Research*, 26, 622-652.

Horn, D.P., and L. Li (2003), Measurement and modeling of gravel beach groundwater response to wave run-up: effects on beach profile changes, *Journal of Coastal Research*, 22(5), 1241-1249.

Izuka, S.K., and S.B. Gingerich (1998), Estimation of the depth to the fresh-water/salt-water interface from vertical head gradients in wells in coastal and island aquifers, *Hydrogeology Journal*, 6(3), 365-373.

Jayatilaka, C.J., and R.W. Gillham (1996), A deterministic-empirical model of the effect of capillary fringe on near-stream area runoff: 1. Description of the model, *J. Hydrol*, 184, 299-315.

Kawabe, M., J. H. Sharp, K.C. Wong, and M.E. Lebo (1988), Density profiles from the Delaware Estuary, *Oceanographic Data Report*, 8, University of Delaware, Newark, Delaware.

King, J.N., A.J. Mehta, and R.G. Dean (2009), Analytical models for the groundwater tidal prism and associated benthic water flux, *Hydrogeology Journal*, 18(1), 203-215, doi:10.1007/s10040-009-0519-y.

Kraft, J. C. (1971), A guide to the geology of Delaware's coastal environments (220 pp.), Newark: College of Marine Studies, University of Delaware.

Li, H., M.C., Boufadel, and J.W. Weaver, (2008), Tide-induced seawater–groundwater circulation in shallow beach aquifers, *Journal of Hydrology*, 352(1-2), 211-224.

Li, L., D.A. Barry, F. Stagnitti, and J.-Y. Parlange (1999), Submarine groundwater discharge and associated chemical input to the coastal sea, *Water Resources Research*, (35)11, 3253-3259.

Li, L., and D.A. Barry (2000), Wave-induced beach groundwater flow, *Advances in Water Resources*, 23, 325-337.

Li, L., D.P. Horn, A.J. Baird (2006), Tide-induced variations in surface temperature and water-table depth in the intertidal zone of a sandy beach. *Journal of Coastal Research*, 22, 1370-1381.

Maurmeyer, E.M. (1974), Analysis of short and long-term elements of coastal change in a simple spit system: Cape Henlopen, Delaware, M.S. Thesis, Department of Geological Sciences, University of Delaware, University of Delaware, Newark, Delaware.

Michael, H.A., A.E. Mulligan, and C.F. Harvey (2005), Seasonal oscillations in water exchange between aquifers and the coastal ocean, *Nature*, 436(7054), 1145-1148.

Miller, D.C., and W.J. Ullman (2004), Ecological consequences of ground water discharge to the Delaware Bay, United States, *Ground Water*, 42(7), 959-970.

Moore, W.S. (2010), The effect of submarine groundwater discharge on the ocean, *Annu. Rev. Mar. Sci*., 2, 59–88.

Nielsen, P. (1990), Tidal dynamics of the water table in beaches, *Water Resources Research*, 26(9), 2127-2134, doi:10.1029/WR026i009p02127.

Paerl, H., L. Valdes, J. Pinckney, M. Piehler, J. Dyble, and P. Moisander (2003), Phytoplankton photopigments as indicators of estuarine and coastal eutrophication, *BioScience*,53(10), 953-964.

Ramsey, K.W., and L.T. Wang (2001), Historical Coastline Changes of Cape Henlopen, Delaware, Delaware Geological Survey Special Publication No. 25.

Riedel, T., K. Lettmann, M. Beck, and H-J. Brumsack (2010), Tidal variations in groundwater storage and associated discharge from an intertidal coastal aquifer, *Journal of Geophysical Research*, 115(C04013).

Robinson, C., B. Gibbes, and L. Li (2006), Driving mechanisms for flow and salt transport in a subterranean estuary, *Geophysical Research Letters*, 33, L03402, doi:10.1029/2005GL025247.

Robinson, C., L. Li, and D. Barry (2007a), Effect of tidal forcing on a subterranean estuary, *Advances in Water Resources*,30(4), 851-865, doi:10.1016/j.advwatres.2006.07.006.

Robinson, C., B. Gibbes, H. Carey, and L. Li. (2007b), Salt-freshwater dynamics in a subterranean estuary over a spring-neap tidal cycle, *Journal of Geophysical Research*, 112(9), 1-15, doi:10.1029/2006JC003888.

Rusch, A., S. Forster, and M. Huettel (2001), Bacteria, diatoms and detritus in an intertidal sandflat subject to advective transport across the water-sediment interface, *Biogeochemistry*, *55*(1), 1-27.

Saiers, J.E., and J.J. Lenhart (2003), Ionic-strength effects on colloid transport and interfacial reactions in partially saturated porous media. *Water Resources Research*, *39*(9), 13.

Santoro, A. (2010), Microbial nitrogen cycling at the saltwater-freshwater interface, *Hydrogeology Journal*, 18, 187-202, dio:10.1007/s10040-009-0526-z.

Santos, I. R., W.C., Burnett, T. Dittmar, I G. N. A. Suryaputra, and J. Chanton (2009), Tidal pumping drives nutrient and dissolved organic matter dynamics in a Gulf of Mexico subterranean estuary, *Geochimica et CosmochimicaActa*, 73(5), 1325-1339, doi:10.1016/j.gca.2008.11.029.

Santos, I.R., W.C. Burnett, T. Dittmar, I.G.N.A Suryaputra, and J. Chanton, (2008), Tidal pumping drives nutrient and dissolved organic matter dynamics in a Gulf of Mexico subterranean estuary, *Geochimicaet Cosmochimica Acta*, 73(5), 1325-1339.

Sharma, M.M., and Y.C. Yortsos (2004), Transport of Particulate Suspensions in Porous Media: Model Formulations, *AlChE Journal*, 33(10), 1636-1643.

Sharp, J.H., C.H. Culberson, and T.M. Church (1982), The chemistry of the Delaware estuary; general considerations, *Limnology and Oceanography*, 27(6), 1015-1028.

Simmons, C.T., T.R. Fenstemaker, and J.M. Sharp (2001), Variable-density groundwater flow and solute transport in heterogeneous porous media: approaches, resolutions and future challenges. *Journal of Contaminant Hydrology*, 52, 245-75.

Taniguchi, M., W.C. Burnett, J.E. Cable, and J.V. Turner (2002), Investigation of submarine groundwater discharge, *Hydrological Processes*, 11, 2115-2129, doi:10.1002/hyp.1145.

Turner, I.L., B.P. Coates, and R.I. Acworth (1997), Tides, waves and the super-elevation of groundwater at the coast, *Journal of Coastal Research*, 13(1), 46-60.

Turner, I. L., and P. Nielsen (1997), Rapid water table fluctuations within the beach face: Implications for swash zone sediment mobility?, *Coastal Engineering*, 32(1), 45-59.

Turner, I. L., and G. Masselink (1998), Swash infiltration-exfiltration and sediment transport,*Journal of Geophysical Research*, 103, 30813-30824.

Valiela, I., J. Costa, K. Foreman, J.M. Teal, B. Howes, and D. Aubrey (1990), Transport of groundwater-borne nutrients from watersheds and their effects on coastal waters; groundwater inputs to coastal waters, *Biogeochemistry*, 10(3), 177-97.

Ullman, W.J., B. Chang, D.C. Miller, and J.A. Madsen (2003), Groundwater mixing, nutrient diagenesis, and discharges across a sandy beachface, Cape Henlopen, Delaware (USA), *Estuarine, Coastal and Shelf Science*, 57, 539-52.

Urish, D., and T.E. McKenna (2004), Tidal effects on ground water discharge through a sandy marine beach, *Ground Water*, 42(7), 971-982

USACE (1996), Rehoboth Beach/Dewey Beach Interim Feasibility Study: Final Feasibility Report and Final Environmental Impact Statement, U.S. Army Corps of Engineers, Philadelphia District, 146 p.

USACE (1997), Roosevelt Inlet-Lewes Beach, DE, Interim Feasibility Study: Final Feasibility Report and Final Environmental Assessment Statement. U.S. Army Corps of Engineers, Philadelphia District, 256 p.

Vandenbohede, A., and L. Lebbe (2005), Occurrence of salt water above fresh water in dynamic equilibrium in a coastal groundwater flow system near De Panne, Belgium, *Hydrogeology Journal*, 14(4), 462–472.

Xin, P., C. Robinson, L. Li, D.A. Barry, and R. Bakhtyar (2010), Effects of wave forcing on a subterranean estuary, *Water Resources Research*, 46, W12505.

Appendix A

FIELD INSTRUMENTATION

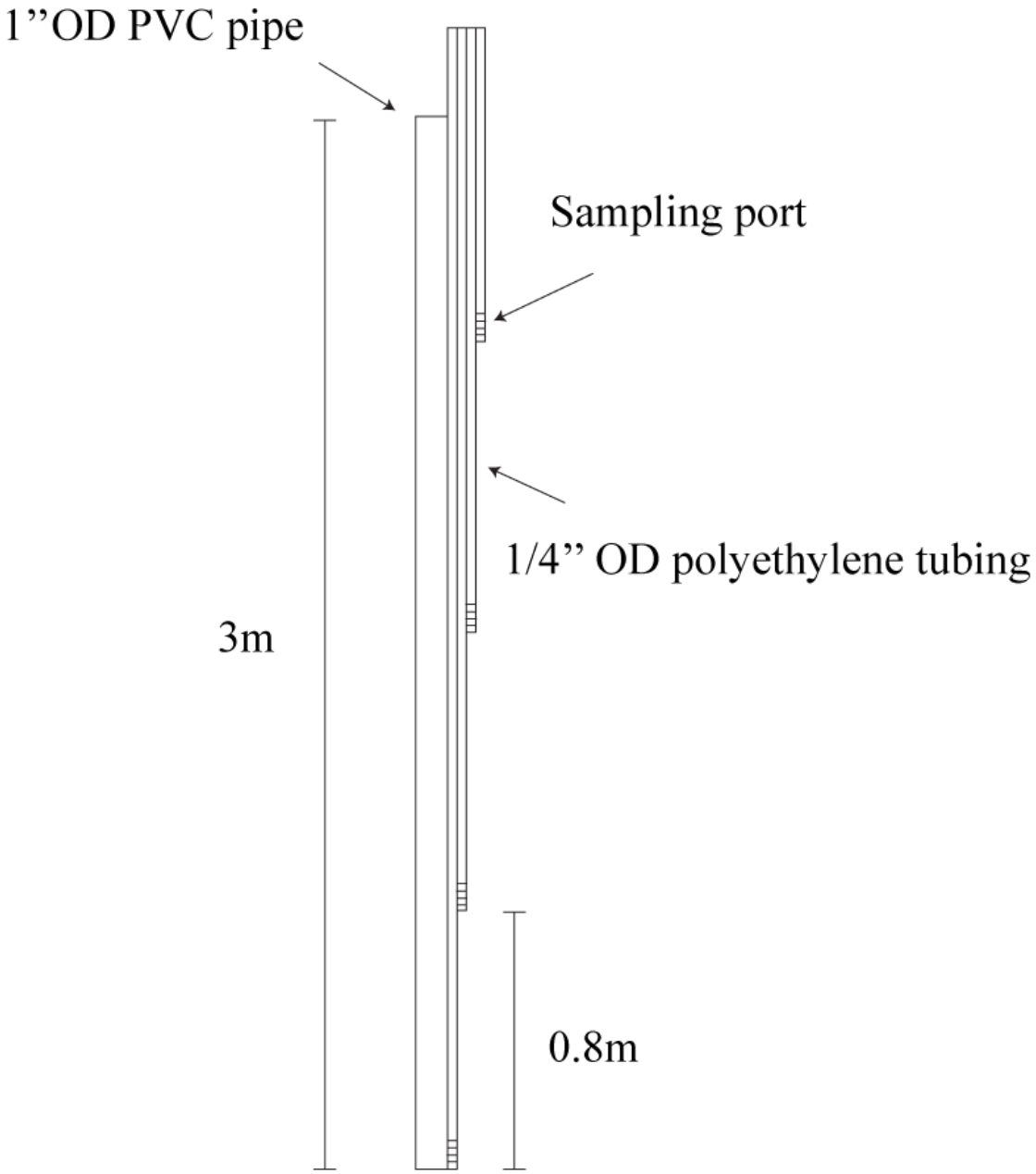

Figure A1. Schematic of multi-level sampler.

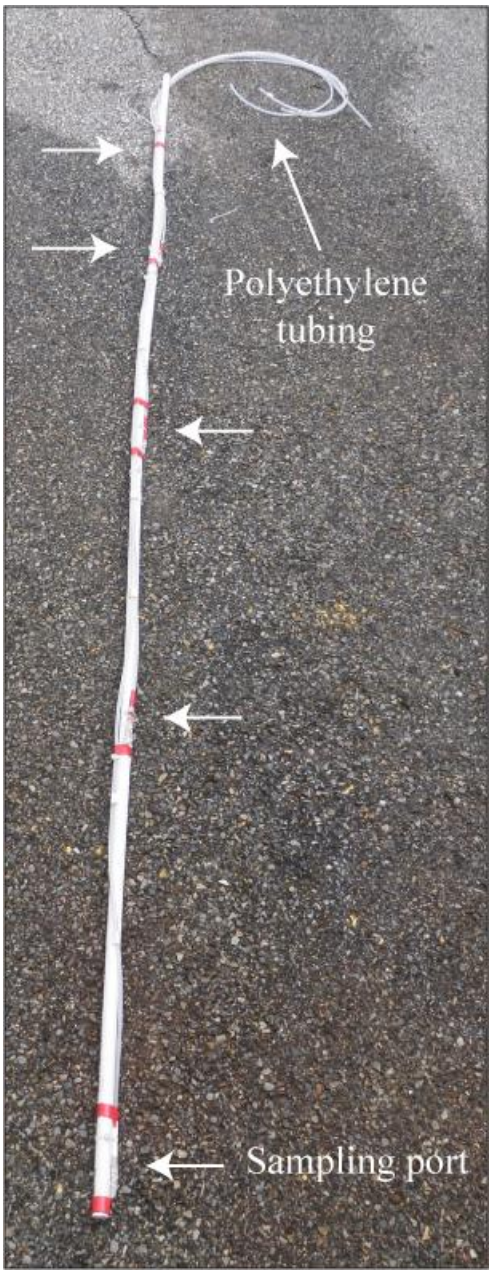

Figure A2. Image of multi-level sampler.

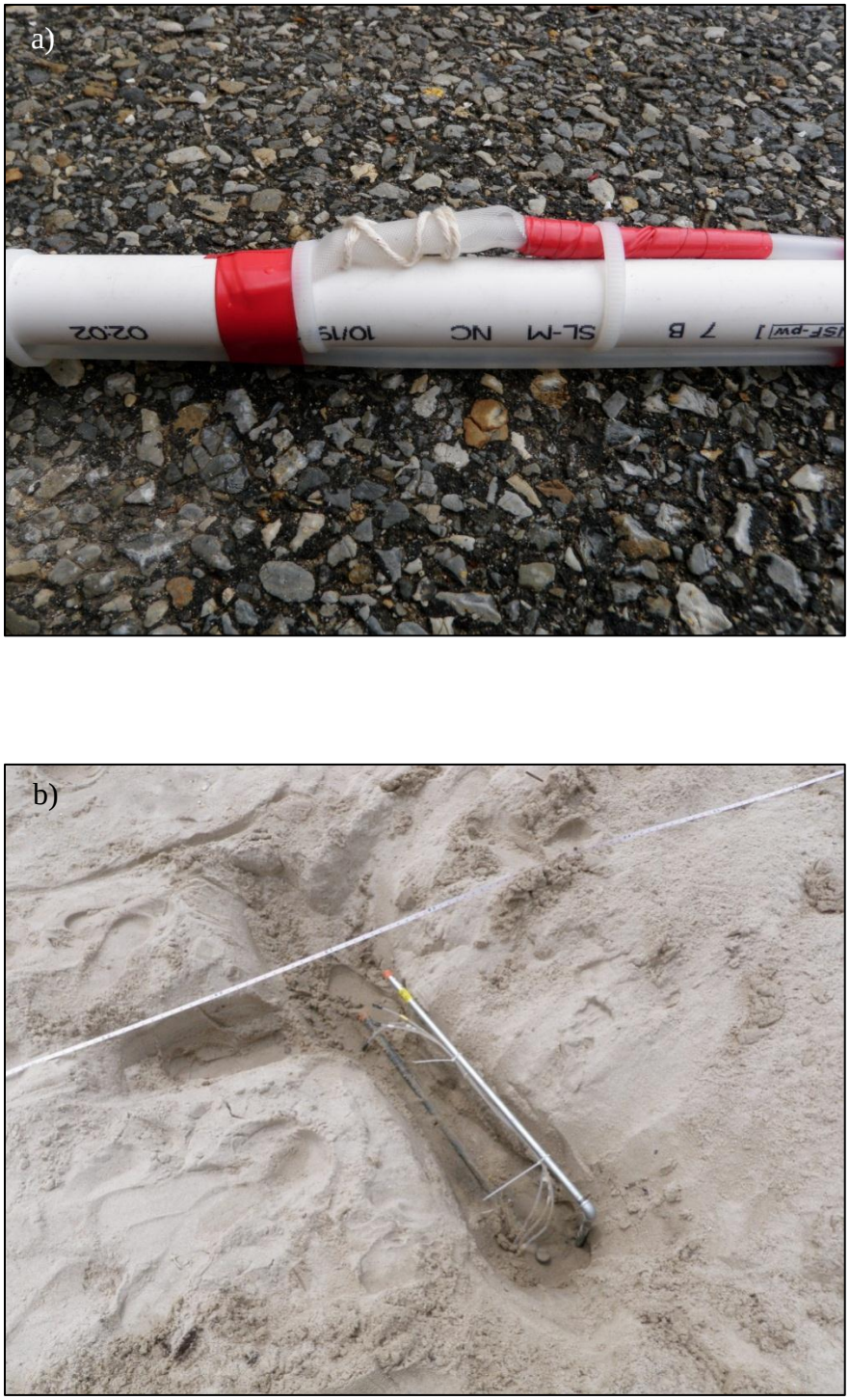

Figure A3. Image of a) sampling port and b) multi-level sampler after installation with tubing attached to steel pipe for retrieval.

Table A1. Sample port elevation and shore-perpendicular position.

Sampling Port	Distance from BM [m]	Height Rel. NAVD88 [m] Summer	Height Rel. NAVD88 [m] Winter
1-1	27.4	-0.167	-0.65
1-2	27.4	-1.4	-1.89
1-3	27.4	-2.545	-3.02
2-1	34.2	-0.305	-0.79
2-2	34.2	-1.195	-1.59
2-3	34.2	-1.83	-2.39
2-4	34.2	-2.805	-3.19
3-1	38.9	-0.7435	-1
3-2	38.9	-1.495	-1.8
3-3	38.9	-2.175	-2.6
3-4	38.9	-2.815	-3.4
4-1	42.86	-1.4455	-1.4455
4-2	42.86	-2.045	-2.045
4-3	42.86	-2.675	-2.675
4-4	42.86	-3.14	-3.14
5-1	49.43	-1.74	-1.74
5-2	49.43	-2.355	-2.355
5-3	49.43	-2.98	-2.98
5-4	49.43	-3.57	-3.57
5-5	49.43	-4.18	-4.18
6-1	56	-2.17	-2.17
6-2	56	-2.68	-2.68
6-3	56	-3.355	-3.355

Appendix B

SIEVE ANALYSIS

Table B1. Cape Shores 0-0.5 m sieve analysis.

Soil Sample:	Cape Shores	Container Weight (g):	26.8
	Mid Beachface (0-0.5m depth)	Container and Dry Soil Weight (g):	607.2
Date:	11.11.2010	Dry Soil Weight (g):	580.4
		% Error:	0.65%

Sieve Number	Sieve Opening (mm)	Sieve Weight	Sieve and Soil Weight	Retained Soil Weight (g)	Percent Retained	Cumulative Percent Retained	Percent Finer
4	4.75	534.8	534.8	0	0.00	0.00	100.00
8	2.38	367.5	367.5	0	0.00	0.00	100.00
10	2	457.3	457.3	0	0.00	0.00	100.00
25	0.707	326.9	427.6	100.7	17.46	17.46	82.54
50	0.297	277.7	685.2	407.5	70.67	88.14	11.86
60	0.25	376.6	417.8	41.2	7.15	95.28	4.72
80	0.177	264.2	288.4	24.2	4.20	99.48	0.52
125	0.125	250.4	253.1	2.7	0.47	99.95	0.05
Pan	-	369.8	370.1	0.3	0.05	100.00	0.00
			Total Retained:	576.6			

Table B2. Cape Shores 0.5-1.0m sieve analysis.

Soil Sample:	Cape Shores	Container Weight (g):	23.2
	Mid Beachface (0.5-1.0m depth)	Container and Dry Soil Weight (g):	593.8
Date:	11.18.2010	Dry Soil Weight (g):	570.6
		% Error:	0.14%

Sieve Number	Sieve Opening (mm)	Sieve Weight (g)	Sieve and Soil Weight (g)	Retained Soil Weight (g)	Percent Retained	Cumulative Percent Retained	Percent Finer
	16	557.3	565.3	8	1.40	1.40	98.60
4	4.75	534.7	631.4	96.7	16.97	18.37	81.63
8	2.38	367.5	430.2	62.7	11.00	27.97	72.03
10	2	457.1	474.8	17.7	3.11	31.08	68.92
25	0.707	328.6	508.8	180.2	31.63	62.71	37.29
50	0.297	279.8	430.3	150.5	26.41	89.12	10.88
60	0.25	377.2	396.6	19.4	3.40	92.52	7.48
80	0.177	264.3	287.7	23.4	4.11	96.63	3.37
125	0.125	250.4	265.9	15.5	2.72	99.35	0.65
Pan	-	369.8	373.5	3.7	0.65	100.00	0.00
			Total Retained:	569.8			

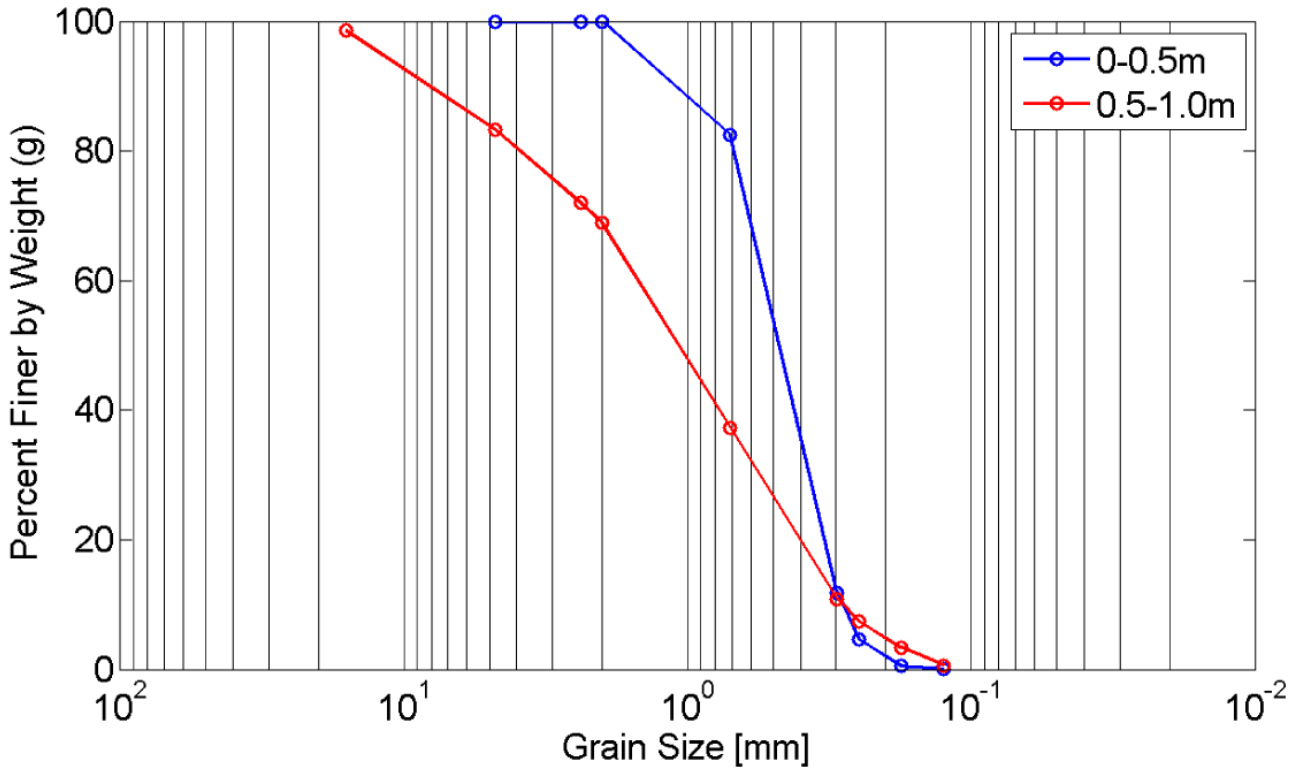

Figure B1. Cape Shores 0.5-1.0m and 1.0-1.5m sieve analysis.

Appendix C

TIDE ELEVATIONS

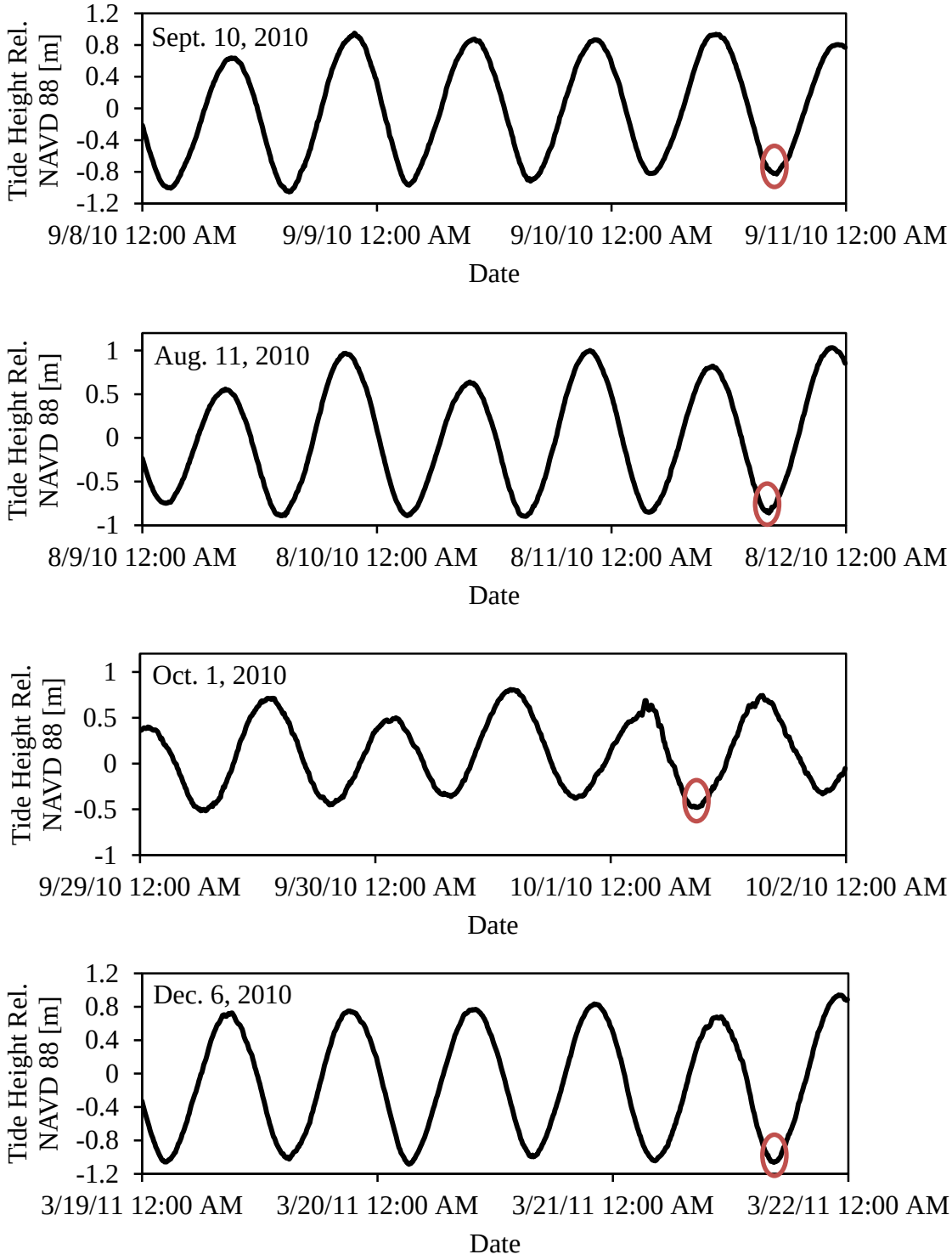

Figure C1. Tide elevation 2 days prior and leading up to porewater sampling events. Time and duration of sampling event circled in red.

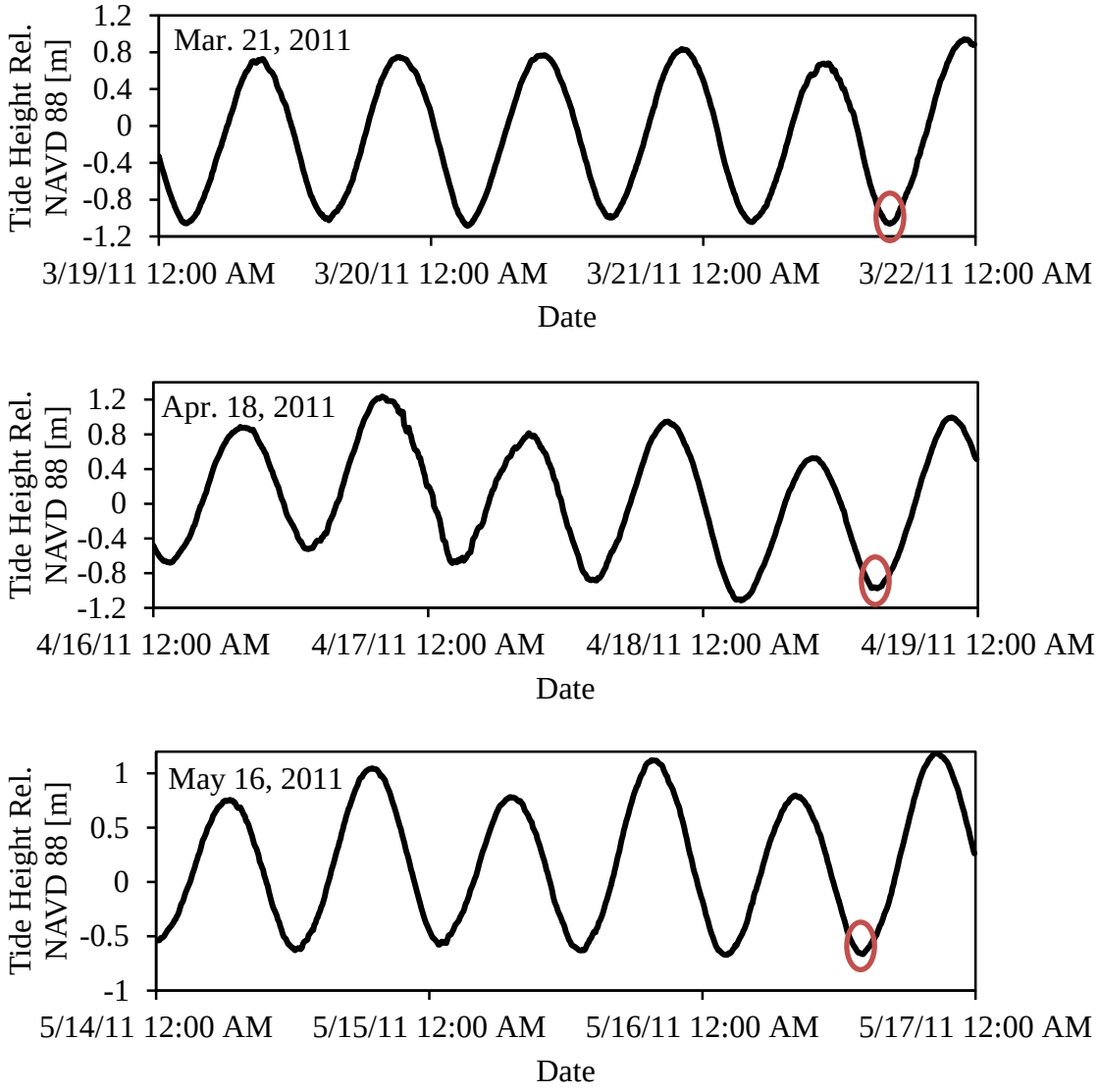

Figure C1. Continued.

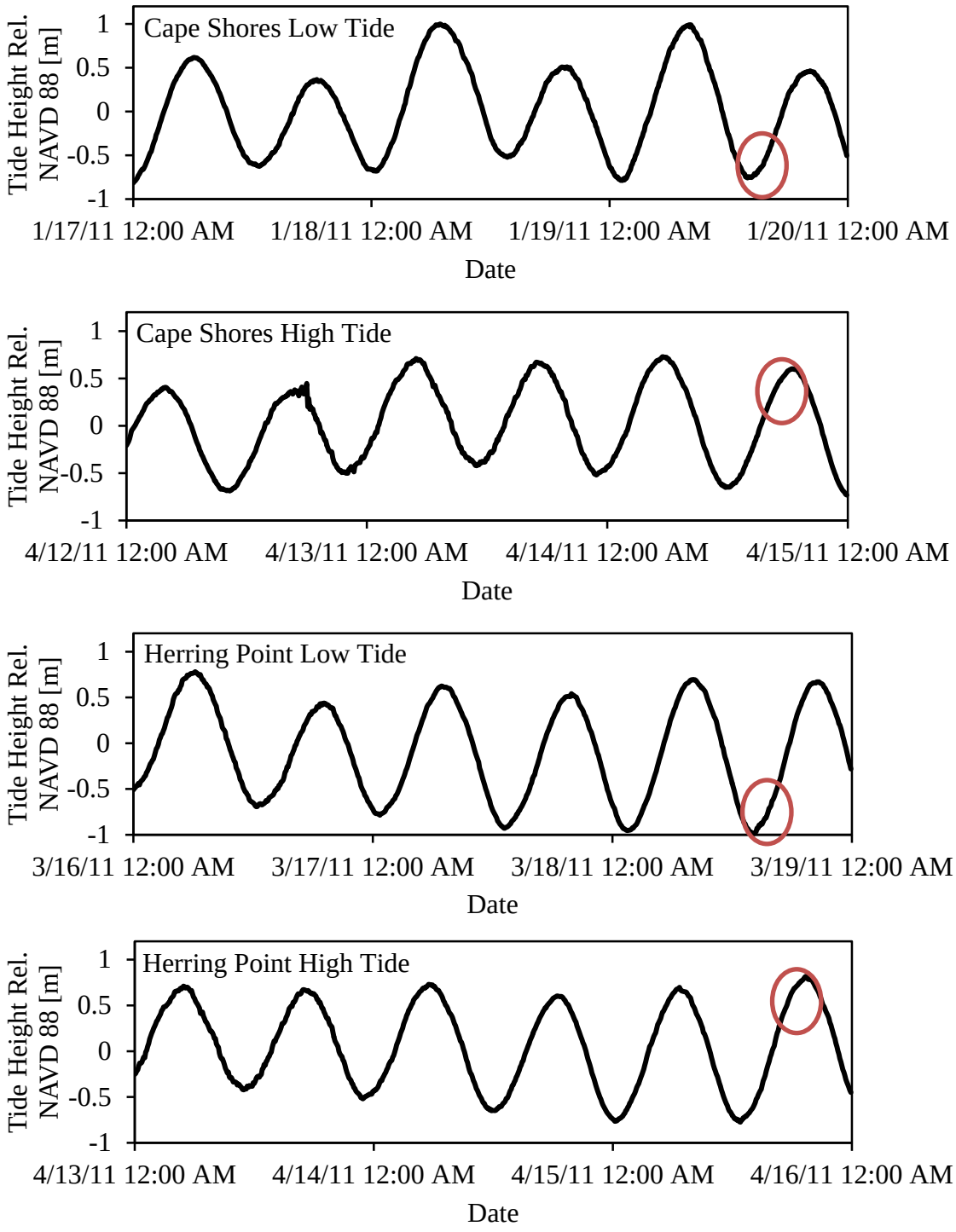

Figure C2. Tide elevation 2 days prior and leading up to sensor experiments. Measurements were recorded during a rising tide circled in red.

Appendix D

DAILY PRECIPITATION TOTALS

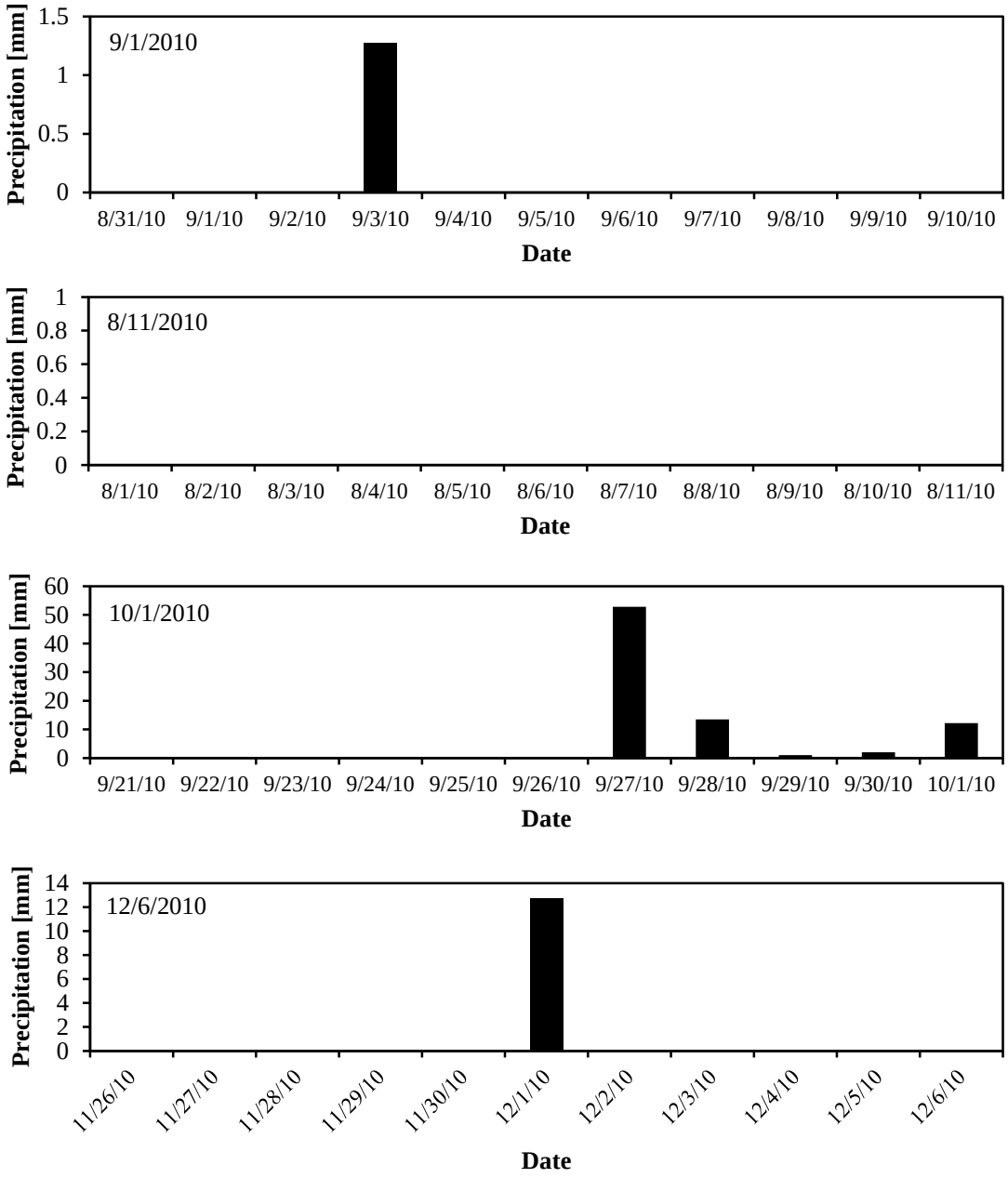

Figure D1. Daily precipitation totals for Lewes, DE 10 days before porewater sampling events.

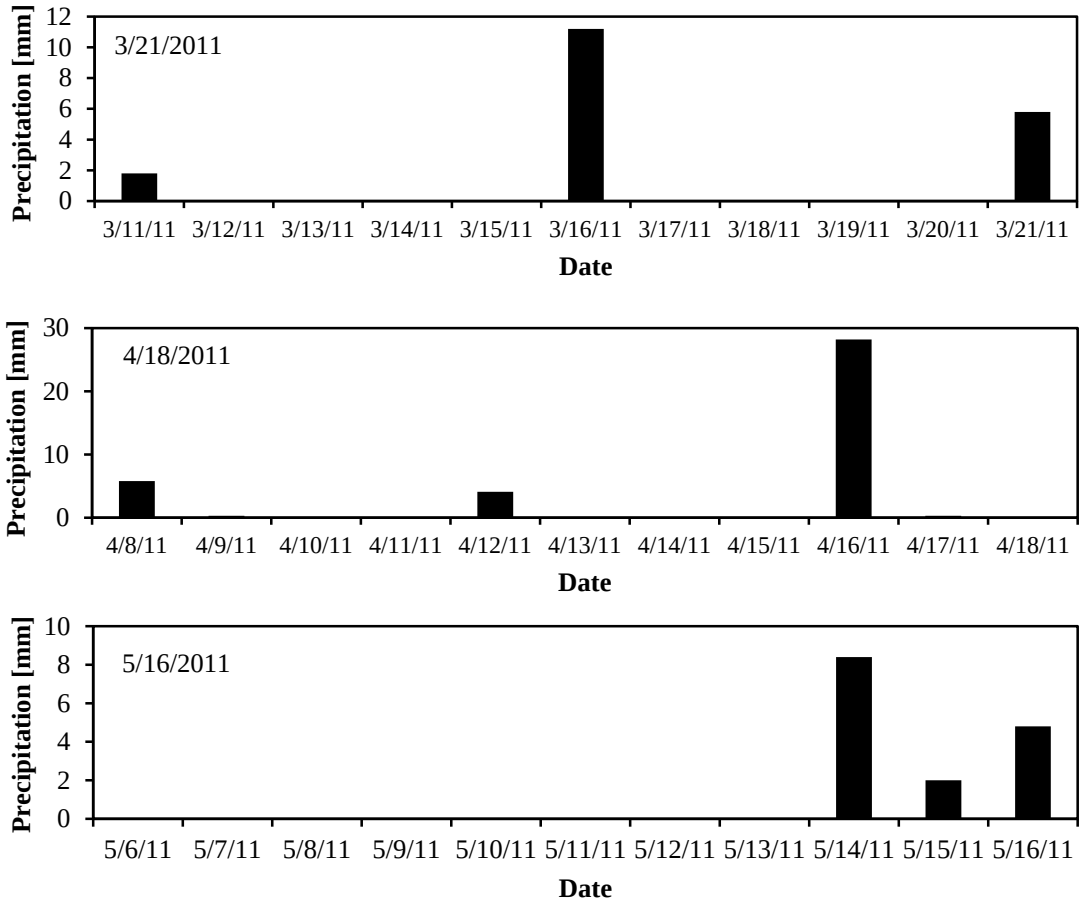

Figure D1. Continued.